ELECTRONIC TRANSPORT AT SEMICONDUCTOR AND PEROVSKITE OXIDE INTERFACES

by

NICHOLAS JAMES GOBLE

Submitted in partial fulfillment of the requirements for the degree of

Doctor of Philosophy

Department of Physics

CASE WESTERN RESERVE UNIVERSITY

May, 2016

CASE WESTERN RESERVE UNIVERSITY

SCHOOL OF GRADUATE STUDIES

We hereby approve the thesis/dissertation of

Nicholas James Goble

candidate for the degree of **Doctor of Philosophy***.

Committee Chair

Xuan P.A. Gao

Committee Member

Harsh Mathur

Committee Member

Kathleen Kash

Committee Member

Alp Sehirlioglu

Date of Defense

December 11, 2015

*We also certify that written approval has been obtained

for any proprietary material contained therein.

To my wife, Mary. Your love and support has made this all possible.

Table of Contents

Chapter 1 Introduction 1

1.1 Introducing quantum mechanics to electronic transport 4

1.1 Two-dimensional electronic systems 5

1.2 Materials of interest 9

1.2a GaAs/$Al_xGa_{1-x}As$ quantum wells 10

1.2b $LaAlO_3/SrTiO_3$ heterointerfaces 16

1.2c γ-$Al_2O_3/SrTiO_3$ heterointerfaces 19

1.3 Structural phase transition in $SrTiO_3$ 20

1.3a Structural phase transitions in two dimensions 21

1.3b Cubic-to-tetragonal phase transition in $SrTiO_3$ 23

Chapter 2 Samples and experimental setup 26

2.1 GaAs/$Al_xGa_{1-x}As$ samples 26

2.2 Perovskite oxide samples 28

2.2a γ-$Al_2O_3/SrTiO_3$ 29

2.2b $LaAlO_3/SrTiO_3$ 29

2.3 Micron-scale fabrication of $LaAlO_3/SrTiO_3$ 30

2.4 Tetragonal domain imaging of $LaAlO_3/SrTiO_3$ 31

2.5 Low-temperature/low-noise electrical transport measurements 32

Chapter 3: Short-range scattering on two-dimensional holes in quantum wells 36

3.1 Scattering mechanisms and the nonmonotonic resistance peak 36

3.2 The effect of quantum wall barrier height on electronic transport 38

3.3 Longitudinal resistance in the Bloch-Gruneisen regime 40

3.4. Characteristic temperature in response to disorder 44

3.5 Universality of the electronic contribution and its implications 45

Chapter 4 Metal-insulator transition in perovskite oxide heterointerfaces 51

4.1 Strontium titanate in an electric field 52

4.2 Gating effects of STO 55

4.3 Immobile charge carriers 57

4.4 Mott insulating behavior 59

Chapter 5 Anisotropic electronic transport in an oxide heterointerface 62

5.1 Cubic-to-tetragonal phase transition in $LaAlO_3/SrTiO_3$ 63

5.2 Phase transitions affecting electronic transport 67

5.3 Anisotropic resistance due to tetragonal domain walls 69

5.4 Electrostatic simulation of domain walls 72

Chapter 6 Summaries and perspectives 75

Bibliography 78

List of Tables

Table 5.1: Collection of patterned and measured samples. All seven samples studied were grown using pulsed laser deposition. A LAO thickness of 10 u.c. provided reliable interfacial conduction in all growth conditions, though a sample with 8 u.c. LAO thickness was studied as well, providing comparable results. Samples grown at a lower O_2 partial pressure showed substantially higher carrier densities due to the increase in oxygen vacancies in the STO crystal. Sample 10a.615 was patterned with eight contacts, allowing for multiple measurement configurations across the same domain wall. 66

List of Figures

Figure 1.1. (a) Energy band structure for two separate materials with different energy gaps. At room temperature, GaAs has a direct band gap of 1.42 eV, while $Al_xGa_{1-x}As$ has a direct band gap of $1.42 + 1.25x$ eV for $x < 0.45$. (b) Energy band bending of GaAs/AlGaAs heterointerface. To reach an equilibrium of the Fermi level, energy bands are bent, forming a triangular quantum well on the GaAs side of the interface. (c) Density of states of a two-dimensional electron gas with only one occupied subband, where $EF < E2$. Inset is the energy levels of a triangular quantum well. 8

Figure 1.2. Zincblende crystal structure of GaAs and AlGaAs. For GaAs, the color of the spheres represents atoms of different types, though the assignment is arbitrary. Without purple spheres, the structure is a basic face-centered cubic (FCC) unit cell. A zincblende structure can be created by overlaying two FCC unit cells (lattice parameter *a*) of different atoms offset by $(a4, a4, a4)$. 11

Figure 1.3. (a) Perovskite unit cell of strontium titanate. An octahedral of oxygen atoms occupy the face centers of the cubic crystal formed by strontium atoms. (b) Cross sectional slice of a 4-unit cell (u.c.) lanthanum aluminate/strontium titanate heterointerface. The junction must be TiO_2-terminated $SrTiO_3$. 17

Figure 1.4. Lattice spacing for a two-dimensional cubic lattice as it transitions to tetragonal. At temperature $T > Tc$, the crystal structure is square (a) with a lattice constant of $a0$. As the temperature is lowered, buckling occurs (b) and the lattice spacing is reduced, $a < a0$. The temperature is lowered past the critical temperature, $T < Tc$, below which the crystal transitions into a triangular structure with a spacing of $a1$. 21

Figure 1.5. (a) Two-dimensional oblique phase with domain D_1. (b) Two-dimensional oblique phase with domain D_2. (c) Tiling rule for domains D_1 and D_2 in the oblique crystal phase. The intersection of crystal domains form a domain wall based on tiling rules. (d) A striped phase of domains D_1 and D_2 forms, resembling a buckling phase. 22

Figure 1.6. (a) Cubic, perovskite structure of strontium titanate at 300K. Blue, green, and red spheres represent strontium, oxygen, and titanium, respectively. Oxygen atoms form an octahedra. (b) In the tetragonal phase, the oxygen octahedra rotates with an angle, θ, and the axis, *c*, orthogonal to the octahedral rotation extends slightly. 24

Figure 2.1. (a) Three-dimensional schematic of a typical GaAs quantum well sample. InZn contacts are placed in a square Van der Pauw pattern and annealed deep below the surface. (b) Layer structure for GaAs quantum wells used. Note the InZn contact diffuses through the upper GaAs layers to make a solid electrical connection to the two-dimensional electron gas. 26

Figure 2.2. (a) Three-dimensional schematic of a typical perovskite oxide heterointerface sample. The schematic is the same for either $LaAlO_3/SrTiO_3$ or gamma-alumina/$SrTiO_3$. Aluminum contacts are wire bonded in a square Van der Pauw pattern, which pierce through the upper oxide to contact the interface. (b) Layer structure for GaAs quantum wells used. Note the InZn contact diffuses through the upper GaAs layers to make a solid electrical connection to the two-dimensional electron gas. 28

Figure 2.3. Sample reduction process. (a) As-is $LaAlO_3/SrTiO_3$ crystal with a conductive two-dimensional electron gas at the interface. After photolithography, a (b) Van der Pauw photoresist mask remains adhered to the $LaAlO_3$ surface. The unmasked $LaAlO_3$ and

underlying $SrTiO_3$ are etched 5-7 nm deep with hydrofluoric acid, removing the two-dimensional conductive interface everywhere except under the Van der Pauw mask. (c) The photoresist mask is removed with acetone, leaving the underlying interface unaffected (d). 30

Figure 2.4. (a) Circuit diagram representing a common 4-wire measurement using lock-in techniques. An AC current source is input to the DUT and measured with a lock-in amplifier, while the corresponding AC voltage is measured with a second lock-in amplifier. A backgate can be charged using a DC voltage source. (b) Circuit diagram representing a standard capacitance measurement with a DC offset. A transformer is used to mix AC and DC signals, which is input to the DUT. A lock-in amplifier measures the AC current drawn by the DUT. 33

Figure 3.1. Longitudinal resistance R_{xx} vs T of two-dimensional holes in a 20-nm-wide GaAs/$Al_xGa_{1-x}As$ quantum well with aluminum mole fractions of (a) 7% and (b) 13% in the $Al_xGa_{1-x}As$ barrier. The dotted lines mark T_0, the position of the peak in $R_{xx}(T)$. 39

Figure 3.2. (a) The temperature dependent resistance, normalized with R_0, for 20-nm-wide GaAs/$Al_xGa_{1-x}As$ quantum well with 7%, 10%, and 13% aluminum mole fractions at p = 1.77, 1.73, and 1.71 $\times 10^{10}$ cm^{-2}, respectively. The model fit of Equation 3.1 is indicated by the solid lines. The inset plots the un-normalized resistance as a function of temperature. (b) Dependence of the strength of the two-dimensional metallicity as defined by the ratio of resistance at the peak of $R(T)$ and residual resistance on the hole density. The error bars come from averaging measurements from different current/voltage configurations and different samples. Zero-bias densities are the maximum densities for each Al%. 41

Figure 3.3. Characteristic temperature T_0 vs two-dimensional hole density for various GaAs quantum wells with different aluminum fractions in the barrier, where T_0 represents the temperature at which $R_{xx}(T)$ peaks. 44

Figure 3.4. The dimensionless, T-dependent part of the electronic contribution to R_{xx}, normalized to the height of the resistance peak in $R_{xx}(T)$, plotted against temperature normalized by the characteristic temperature T_0. 46

Figure 3.5. Low temperature ($T \longrightarrow 0$) mobility as a function of backgate-controlled hole density in 20-nm-wide GaAs quantum wells with different aluminum mole fractions in the $Al_xGa_{1-x}As$ barrier. Different symbol colors correspond to different x in the $Al_xGa_{1-x}As$ barrier (orange: x = 7%; black: x = 10%; green: x = 13%), and different symbol shapes correspond to different samples or current-voltage configurations. The dashed lines are a guide to the eye. 49

Figure 4.1. Temperature dependence of the dielectric constant of strontium titanate [001] in electric fields applied with a back gate. Electric field dependence is greatly enhanced below 65 K. Reprinted from "Permittivity of strontium titanate." By R. C. Neville, B. Hoeneisen, and C. A. Mead, *Journal of Applied Physics* 45(5), 2124-2131 (1972). 54

Figure 4.2. Back-gated perovskite oxide heterointerface. A positively charged conductive backgate polarizes the strontium titanate substrate, inducing a change in the charge carrier density at the interface. 55

Figure 4.3. Gate voltage dependence on carrier density at a γ-$Al_2O_3/SrTiO_3$ interface. Measurements (shown in black) were collected with Hall measurements while increasing V_g. Calculations were completed using predictions to the carrier density given by the

parallel plate capacitor model, added to $n(V_g = 0\ \text{V})$. A difference between measured values and calculated values is shown at 30 K (a), 50 K (b), and 100 K (c). (d) Gate voltage dependence of capacitance of the $SrTiO_3$ on a γ-Al_2O_3/$SrTiO_3$ sample at 10 K. Hysteric behavior is expected due to the polarizability of strontium titanate. 56

Figure 4.4. Temperature dependent resistance of a γ-Al_2O_3/$SrTiO_3$ interface. The sample is backgated with an increasing voltage from -30 V to 100 V. 60

Figure 5.1. Overview of cubic-to-tetragonal phase transition in LAO/STO. (a) TEM image of LAO/STO interface. Imaged sample has 10 unit cells of LAO and was grown in 10^{-4} Torr O_2 partial pressure. (b) Polarized transmission microscopy images of LAO/STO showing tetragonal domains at different temperatures. Tetragonal domain walls disappear between 97 K and 100 K. (c) Temperature dependent resistance of an etched 10 u.c. LAO/STO sample. Arrows indicate temperature sweep direction, showing hysteresis below the transition temperature. Insets show temperature dependent resistance from 2 K – 300 K and polarized microscopy images of the sample in the tetragonal and cubic phases. 65

Figure 5.2. Striped tetragonal domain imaging through thermal cycling. Multiple LAO/STO samples were imaged through the structural phase transition prior to patterning and etching. Samples were carefully heated from 77 K to 125 K and subsequently cooled back down to 77 K. No change in the domain wall configuration was observed due to thermal cycling through the cubic-to-tetragonal phase transition..... 67

Figure 5.3. Normalized temperature dependent resistance for a 10 u.c. LAO/STO sample before (a) and after (b) etching. R_1 and R_2 indicate perpendicular current orientations (see

inset). Inset is a standard microscopy image of the etched Van der Pauw pattern. The process of etching the sample is shown in (c). A photoresist mask is patterned on bare LAO/STO, which is subsequently etched. The mask is removed, leaving only the conductive interface covered by the pattern. After the process is complete, the sample topography was imaged using an optical profilometer (d). 68

Figure 5.4. Tetragonal domain overlays and corresponding temperature dependent resistance. (a, b, c) Conductive Van der Pauw patterns created using photolithography and wet etching are outlined in white. Images and data show samples at 77 K with no domain walls, a domain wall at 90°, and a domain wall at 45°, respectively. Images (d, e, f) show the normalized temperature dependent longitudinal resistance for two measurement orientations. Resistance is isotropic with no domain wall (a) and a 45° wall (c) and is anisotropic with a 90° domain wall (b). All samples are 10 u.c. thick and grown at 10^{-4} Torr O_2 pressure. 70

Figure 5.5. Anisotropy strength in various LAO/STO samples split by a domain wall at 90°. All samples are 8-10 u.c. LAO thick and grown at 10^{-5} or 10^{-6} Torr O_2 pressure. Samples with a 90° domain wall show an anisotropy of 1-6 orders of magnitude between $R_{parallel}$ and $R_{perpendicular}$. Y-axis scale has been reduced for clarity..... 71

Figure 5.6. Simulated current flow and voltage distribution for inhomogeneous 20 μm × 20 μm Van der Pauw patterns. The conductive squares are split by 10 μm wide regions with different resistivity, where ρ_1 = 25,000 Ω and ρ_2 = 10,000 Ω. Total current flow is 10 nA in all simulations and is represented with streamlines. Simulated samples in (a) and (b) are split by more conductive regions oriented perpendicular and parallel to the current flow,

respectively. When a conductive region splits the sample, measured $V_{parallel}$, and therefore $R_{parallel}$ is greater than $V_{perpendicular}$ and $R_{perpendicular}$, and the sample shows enhanced conductance perpendicular to the conductive region. However, when the samples are split by a more resistive area as in (c) and (d), the sample shows enhanced conduction parallel to the more resistive region..... 73

Acknowledgements

There are numerous people, without whom this dissertation would not have been possible. Their collaboration, guidance, and support have left a permanent impact on my career.

My research advisor, Dr. Xuan P.A. Gao is most responsible for my success in my graduate career. At the beginning of 2012, he sold me on experimental condensed matter physics and asked me to join his research team. At the time, I was heavily debating between theoretical or experimental condensed matter research, and I struggled to choose between each path. Many nights of sleep were lost due to this decision, as it was a major fork in my career path, and I ultimately choose experiment. Retrospect has shown me this was the right decision, which is largely due to Xuan's mentoring capabilities, experimental expertise, and general knowledge of physics. If my experimental skillset is something to be proud of, it is due to Xuan's sculpting capabilities.

I would like to thank the members of my Ph.D. committee, Dr. Harsh Mathur, Dr. Alp Sehirlioglu, and Dr. Kathy Kash for their effort, helpful advice, and insightful discussions, which have helped me convey scientific concepts more clearly.

None of my work on gallium arsenide quantum wells would have possible without the help of my collaborators Dr. Michael Manfra and Dr. John Watson at Purdue University. They generously donated their time and resources growing custom gallium arsenide quantum wells using their molecular beam epitaxy system, which led to my first, first author manuscript. Additionally, John gave me incredible insight into an experimentalist's understanding of scattering mechanisms in two-dimensional systems.

Dr. Alp Sehirlioglu and Richard Akrobetu from the Department of Materials Science at Case Western Reserve University have grown and provided lanthanum aluminate/strontium titanate heterointerfaces for insightful collaborations. I am grateful for their helpful discussions and nearly endless supply of measurable samples, which have led to many successful results in the field of perovskite oxide heterostructures. In the same regard, Hicham Zaid and Dr. Marie-Helene have been excellent sources of information and wonderful collaborators on $LaAlO_3/SrTiO_3$ systems. The perspective from a materials scientist is not often seen in physics, but I consider it an invaluable tool for interpreting my own research.

Collaborators Dr. John Ekerdt, Dr. Alexander Demkov, Dr. Thong Ngo, Kristy Kormondy, and Bryce Edmondson at the University of Texas at Austin provided countless perovskite oxide heterointerfaces for study, leading to at least two publications that opened new avenues for growing and studying these complex systems. The work would not have been possible without their constant effort and timely sample growths.

I would like to thank the past scientists in my research group, including Dr. Dong Liang, Dr. Juan Du, Dr. Hao Tang, Stephen Fleming, Mike MacDonald, Dr. Zhenhua Wang, Dr. GheeHeui Lee, Dr. Goudong Li, Dr. Richard Qiu, and Yanyuan Zhao for their contributions. They spent countless hours perfecting techniques that were handed down to me and made my research more efficient. I only hope that the expertize I leave will build on theirs and help future generations of Xuan's students.

I would like to thank my current research colleagues and friends, Sukrit Sucharitakul and Shuhao Liu for their support, guidance, and helpful discussions in and out of the laboratory. They sacrificed hours in order to assist my research, from photolithography in

the cleanroom to metal deposition. More valuable though, have been their general attitudes towards research and their uplifting personalities in lab. Their presence has a noticeable, positive effect on my work environment.

I would like to thank the department secretaries Georgia Wilkins, Lori Morton, and Betty Gaffney for their assistance throughout my graduate career. Their behind-the-scenes support keeps the entire department running smoothly, including my research.

Lastly, I finally have the pleasure to formally thank the two members of the department responsible for my pursuit of a graduate degree. Dr. Philip Taylor and Dr. Kathleen Kash. Phil introduced me to graduate level research in 2010, and gave me a glimpse of what graduate research looks like. He is a joy to work with, and I would not be at Case Western Reserve University, let alone in a graduate program, without his recommendation and encouragement. If I completed a second Ph.D., it would be with Phil. Kathy encouraged me to pursue further studies as well, guiding me through the application process and giving me all the more encouragement and confidence to succeed in a Ph.D. program. Her guidance and personal avocation ensured my success in my first-year coursework.

Electronic Transport at Semiconductor and Perovskite Oxide Interfaces

Abstract

by

NICHOLAS JAMES GOBLE

The work discussed in this thesis represents the accumulation of research I performed throughout my doctoral studies. My studies were focused towards two-dimensional electronic transport in semiconductor and perovskite oxide interfaces. Electronic materials with low dimensionality provides experimentalists and theorists with incredible systems to probe physics at non-intuitive levels. Once considered "toy problems," low-dimensional systems, particularly in two dimensions, are now treated as highly relevant, modern electronic materials on the verge of being used in next-generation technology. This thesis entails three main parts, each contributing new knowledge to the field of two-dimensional electronics and condensed matter physics in general.

The first part, found in Chapter 3, analyzes short-range scattering effects in two-dimensional GaAs/AlGaAs quantum wells. The effect of aluminum concentration in the material is correlated to the non-monotonic resistance behavior at low temperatures through the short-range disorder potential. By accounting for different electronic scattering mechanisms, temperature-dependent resistance is shown to have a universal behavior, independent of short-range scattering.

Chapters 4 transitions from two-dimensional electron gasses in GaAs to quasi-two-dimensional electron gasses in perovskite oxides, specifically γ-Al_2O_3/$SrTiO_3$ heterointerfaces. For the first time in that system, a metal-to-insulator transition is measured by backgating the strontium titanate. By measuring the carrier density, it is shown that immobile charge carriers are induced through backgating. Chapter 5 discusses my research on the cubic-to-tetragonal structural phase transition in $LaAlO_3$/$SrTiO_3$ heterointerfaces. By engineering micron-scale devices, I was able to measure the electronic transport properties of tetragonal domain walls below the structural transition temperature. Domain walls are shown to cause anisotropic resistance, which is measurable on small-scale devices.

These three studies significantly contribute to the understanding of two-dimensional electronic transport. They elucidate scattering mechanisms at low temperatures, tuning of the metal-to-insulator transition in a perovskite oxide, and electrical transport through grain boundaries. Overall, this work continues to push our knowledge of two-dimensional systems further, toward achieving a complete understanding of low-dimensional transport in complex systems.

Chapter 1: Introduction

Phase transitions are a core concept in physics – any undergraduate curriculum without substantial phase transition content would be severely lacking. The water cycle is taught from a young age, clearly demonstrating an abstract physical concept in a relatable way. And although seemingly simple, phase transitions describe elementary concepts such as ice melting, to incredible phenomena such as the Big Bang. They continue to provide a powerful framework in which most all of physics can be quantified. Specific to condensed matter physics, the transition between many-body electron states is intriguing. Physicists use this tool to probe the nature of electrons and their behavior in solids. Just like water molecules can cease movement and freeze into a solid, electrons can freeze into a Wigner crystal, freezing into an insulating electronic state. And just as water molecules can warm up and transition to a gaseous state, systems of electrons can form electron gasses or liquids, leading to what is referred to as a metallic state. The phase transition of electrons from a delocalized to localized (mobile to immobile) state is generally referred to as a "metal-to-insulator transition."

The parallels between water and electronic states are limited, but a useful introductory tool to explain condensed matter concepts such as electronic phase transitions. However, the electronic phase transition contains much richer, fundamental physics that are not present in elementary classical phase transitions. Instead of a molecule, it deals with the nature of a fundamental particle. And instead of a classical particle with a collapsed, localized wave function, it can include quantum effects. Additionally, the aspect of a charged particle adds an extra, novel element that increases the complexity of this system,

adding an interparticle interaction term to relevant theories. Initial metal-insulator transition studies neglected the interaction between charge carriers.

1.1 Introducing quantum mechanics to electronic transport

In a disordered electronic system, a complete description of the electrical conductivity cannot be described by classical mechanics alone. Intuitively, this makes sense – the more we decrease the length scale of a physical system, the harder it is to ignore quantum mechanical effects. Since electrical conductivity is studied by considering interparticle spacings on the order of angstroms, it is reasonable to expect a quantum correction to the classical conductivity.

The Drude model of electrical conductivity explains electron transport in metals. Proposed by Paul Drude in 1900, it quickly proved its validity through experiment and is a building block of solid state physics. The Drude model applies kinetic theory to the behavior of electrons in a lattice of heavy disorder potentials, assuming the electrons to behave classically. The model treats electrons as identical yet distinguishable, and applies Maxwell-Boltzmann statistics to charge carriers. Conductivity is calculated by summing up all processes impeding electron flow as a mean relaxation/scattering time. However, it took until the mid-1920s for modern developments in quantum mechanics to arise. From quantum theory, we know that electrons are fermions and obey Fermi-Dirac statistics.

In 1933, Arnold Sommerfeld added to Drude's results by applying quantum mechanics to the classical formalism, giving birth to the Drude-Sommerfeld model. This model retains almost all aspects of the Drude model with the following modifications: Fermi-Dirac statistics are obeyed, energies are discretized, and states are distributed as per the Pauli exclusion principle. This new model proved successful beyond Drude's original model.

However, as far as quantum corrections are concerned, the Drude-Sommerfeld model is still incomplete and regarded as a semi-classical model.

1.1 Two-dimensional electronic systems

A two-dimensional electronic system is one where charge carriers – either electrons or holes – are confined to a plane. When charged particles live in two dimensions, the physical laws governing their behavior are different and arguably more complex. Naïvely, one may expect the elimination of a degree of freedom to reduce the complexity of the physics by 1/3rd, but this is certainly not the case. Historically, emergent physical phenomena have a habit of revealing themselves in two-dimensional systems.

For example, Anderson et al. published a seminal manuscript in 1979 describing electronic localization in 3-, 2-, and 1-dimensional systems, which denied the possibility of a metallic state ($R \rightarrow 0$ as $T \rightarrow 0$) in two dimensional systems[1]. For some time, it was believed that there was no true metallic behavior in two dimensional systems. In 1994, S. Kravchenko *et al*. in Pudalov's group published beautiful data on the temperature-dependent resistance, *R(T)*, in Si-MOSFETs, showing a clear, gate-induced metal-to-insulator transition at 50 mK.[2] This metal-to-insulator transition was also observed in both p-type[3] and n-type[4] GaAs quantum wells in 2003. The disagreement between Anderson's scaling theory of localization and the clear experimental evidence of a metallic state led to a large controversy in the condensed matter community – who was right?

About twenty years after the experimental observation of a 2D metal-to-insulator transition in Si-MOSFETs, the majority of the field believe that the transition is a genuine one, and Anderson localization, although elegant and insightful, was proved to be incomplete. With many-body systems come large approximations, since they are inherently

difficult to solve analytically or numerically. What the theory failed to consider was electron-electron interactions that gave rise to many-body behavior. The interplay between interactions and disorder revised the belief that two-dimensional electronic systems are fundamentally insulating. Metallic states in two dimensions can exist, thanks in full to interactions.

Another two-dimensional phenomenon not predicted by theory is the fractional quantum Hall effect. The integer quantum Hall (IQHE), which is the quantization of the classical Hall resistance due to the quantization of electron orbital energies in a magnetic field, was predicted in 1975[5] and realized in 1980.[6] Two years after the observation of the IQHE, experimentalists working on high mobility GaAs quantum wells noticed additional steps in the Hall resistance not predicted by the IQHE. The observed steps occurred at fractional Landau levels and became known as the fractional quantum Hall effect (FQHE).[7] It took a short time for theorist Robert Laughlin to describe the effect,[8] who soon after shared the 1998 Nobel Prize with the experimentalists Horst Stormer and Daniel Tsui. While the integer quantum Hall effect depends simply on the quantization of single particle energy levels, the fractional quantum Hall effect instead depends on many-body effects of charge carriers. As a result, it is much more observable in systems with high electron-electron correlations. This was one of the most unexpected discoveries in the history of physics, which provided incredible insight into many-body interactions in two dimensions. Again, experimentalists observed incredibly important physics in two-dimensional systems that were not predicted by theory.

Thus, two-dimensional electronic systems are important to consider, not just to discover new physics, but also to keep theorists on their toes. But how are two-dimensional

electron systems engineered, and how are electrons confined to low-dimensional systems? Naively, one may suggest to create an atomically thin plane of metal – copper, for example. Since the metal extends in two dimensions, the electrons should live in two dimensions. However, the electronic band structure of most materials (especially metals) and the overlapping of the Fermi level and the conduction band would give rise to 3-dimensional behavior. Mere spatial confinement is not required to guarantee reduced dimensionality; electrons can be confined by taking advantage of their quantum mechanical wave properties and discrete energy level formation when the size of the system reaches a level comparable to the electron wave length.

In order to energetically confine electrons to a two-dimensional plane, energy band bending must occur. Take GaAs and AlGaAs, for example. Separately, they both have different, but direct band gaps. Through use of modulation doping, the Fermi level in AlGaAs can be tuned to either n-type or p-type (n-type in the case of Figure 1.1a). When brought together, the Fermi energy discontinuity at the interface, which is an unstable state, causes electrons to flow from doped AlGaAs to undoped GaAs. Equilibrium is reached through band bending and 2D electrons are trapped inside the triangular potential well at the interface, which is shown in Figure 1.1b. This is how triangular quantum wells are formed, as long as the energy depth of the well is greater than the energy of the conductive subbands. A second interface of AlGaAs would be needed to create a square quantum well.

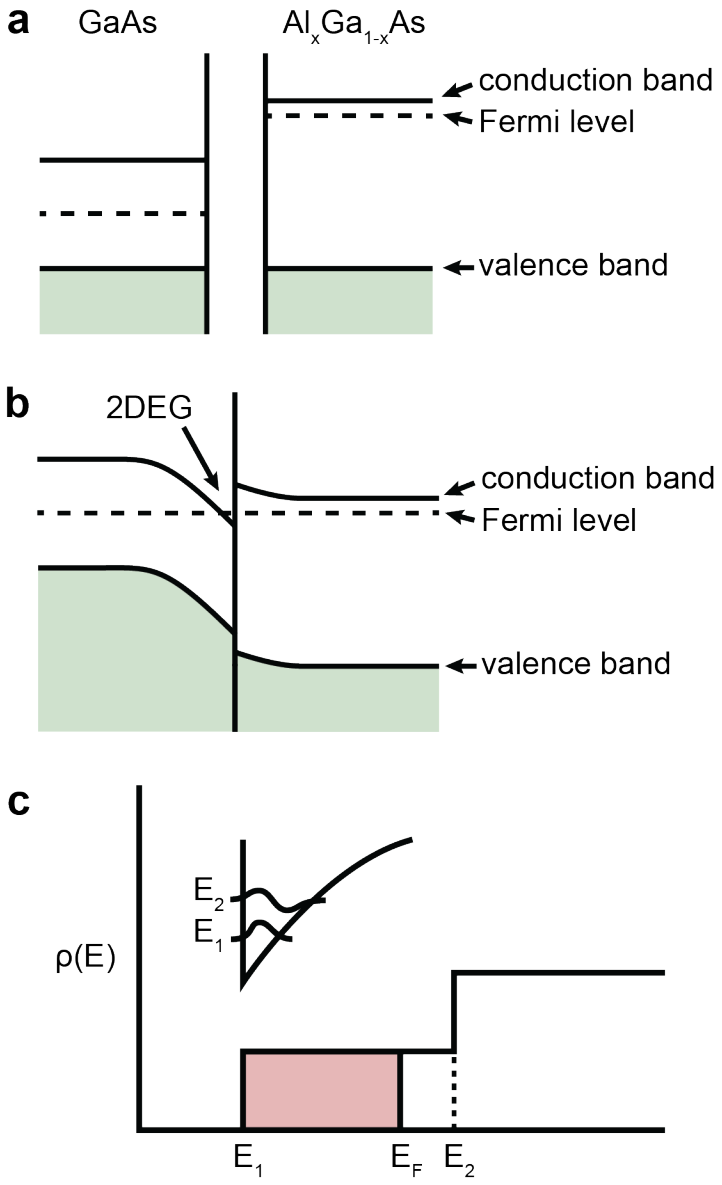

Figure 1.1. (a) Energy band structure for two separate materials with different energy gaps. At room temperature, GaAs has a direct band gap of 1.42 eV, while $Al_xGa_{1-x}As$ has a direct band gap of $1.42 + 1.25x$ eV for $x < 0.45$. (b) Energy band bending of GaAs/AlGaAs heterointerface. To reach an equilibrium of the Fermi level, energy bands are bent, forming a triangular quantum well on the GaAs side of the interface. (c) Density of states of a two-dimensional electron gas with only one occupied subband, where $E_F < E_2$. Inset is the energy levels of a triangular quantum well.

The density of states in a two-dimensional electron system is tied directly to the population of subbands. When only one subband is filled, a two-dimensional electron gas

is formed. When two or more subbands are populated, the system is known as a quasi-two-dimensional electron gas. Two-dimensional effects may still be observed in quasi-two-dimensional systems, but the effects are weaker than in pure, two-dimensional systems. If more than one subband is full, the density of states of the system increases with a step function, instead of a continuously increasing function for three dimensions. The density of states for the first subband is defined as

$$N(E) = \frac{m^*}{\pi\hbar^2}, \qquad \text{Equation 1.1}$$

where m^* is the effective mass. As more subbands are filled, the density of states is multiplied by a step function $\Theta(E - E_n)$, where E_n is the energy of the *n*th subband. Figure 1.1c illustrates the density of states of a two-dimensional electron system with only one subband occupied.

1.2 Materials of interest

Throughout this dissertation, two classes of materials will be discussed – two-dimensional semiconductor quantum wells and quasi-two-dimensional perovskite oxide heterointerfaces. Although both materials exhibit two-dimensional electronic transport, the similarities stop there. Semiconductor quantum wells, specifically GaAs quantum wells, are known for their world record high electron mobility at low temperatures, giving experimentalists a means to study incredible two-dimensional behavior, such as the fractional Quantum Hall effect and its exotic Bose-Einstein condensate states. Perovskite oxide heterointerfaces are of recent interest to the physics community, being discovered only in 2004.[9] Most famously, thin films of lanthanum aluminate exhibit quasi-two-dimensional conductivity when deposited on strontium titanate with proper surface

termination. Despite their relatively new status, a plethora of novel physics has been observed in these systems, and their popularity is still on the rise. This dissertation will present new electrical transport phenomena found in both systems.

1.2a GaAs/$Al_xGa_{1-x}As$ quantum wells

Gallium arsenide/aluminum gallium arsenide triangular quantum wells are made by creating an atomically resolved interface of the two materials using epitaxial growth. In terms of a free electron picture, the system is as close to an even background coulomb potential as one could hope to achieve, due to the low substrate disorder potential and extremely small lattice mismatch between GaAs and AlGaAs. Both GaAs and AlGaAs have zincblende crystal structures, as illustrated in Figure 1.2. The unit cell can be conceptualized as two FCC unit cells of different atom types with lattice parameter a, offset by $(\frac{a}{4}, \frac{a}{4}, \frac{a}{4})$. In the case of $Al_xGa_{1-x}As$, a percentage of gallium atoms, x, is replaced by aluminum atoms.

In GaAs/AlGaAs quantum wells, low temperature charge carrier mobilities of over 3.3×10^7 cm^2/Vs can be achieved, mostly due to modulation doping and advances in molecular beam epitaxy procedures. To put that into perspective, electron mobilities that high have mean free paths of around ~ 300 μm, close to half a millimeter. Years of research dramatically improved the mobilities of these systems, from 10^4 cm^2/Vs in 1978 to 10^7 cm^2 in 1998. Modulation doping was a significant advancement that reduced the effect of ionized donor scattering (a dominant effect at low temperatures). By spatially separating dopants (typically Si or C for n-type and p-type respectively) from the interface, usually between 20 nm – 120 nm, the Coulomb potentials created by ionized donors are greatly reduced, thereby reducing large angle backscattering in the electron gas. Since the electron

mobility is so great, different scattering mechanisms more intrinsic to electronic transport can be studied more efficiently.

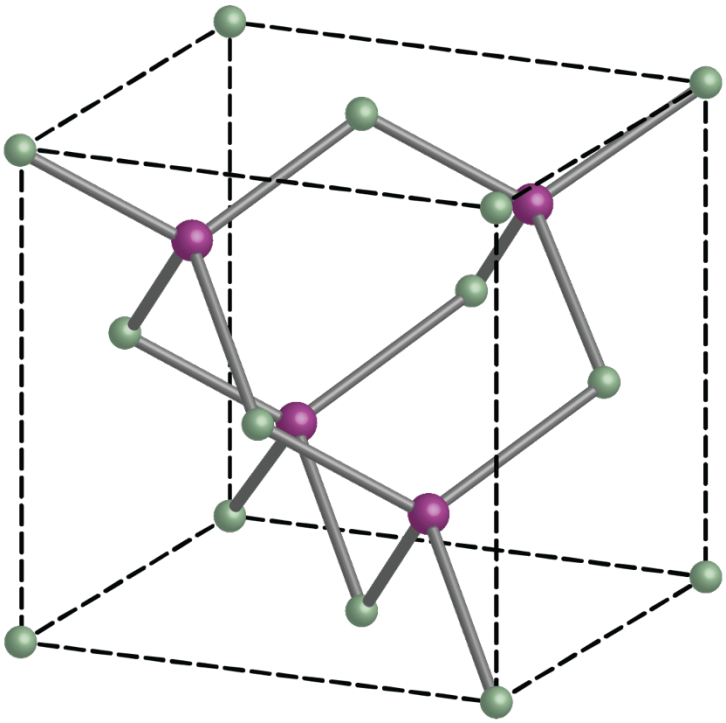

Figure 1.2. Zincblende crystal structure of GaAs and AlGaAs. For GaAs, the color of the spheres represents atoms of different types, though the assignment is arbitrary. Without purple spheres, the structure is a basic face-centered cubic (FCC) unit cell. A zincblende structure can be created by overlaying two FCC unit cells (lattice parameter a) of different atoms offset by $(\frac{a}{4}, \frac{a}{4}, \frac{a}{4})$.

Gallium arsenide quantum wells can be engineered to be either n-type or p-type. There are benefits to both, but experimentalists have undoubtedly shown preference towards n-type due to its record electron mobility and ease of engineering. Diffusion of modulation dopants for p-type GaAs quantum wells was a problem in the past, but has been largely solved with the use of carbon for modulation doping. In addition, the formation of ohmic contacts is widely considered to be a more difficult task in p-type GaAs. Despite the

troubles, p-type GaAs has its benefits. Unlike electrons in GaAs quantum wells, charge carrying holes have a higher effective mass, which leads to stronger inter-particle interactions. Therefore, p-type GaAs/AlGaAs quantum wells are used to study two-dimensional physics where strong correlations play a dominant role, such as the fractional quantum Hall effect and the metal-insulator transition.

There are a variety of possible scattering effects in GaAs quantum wells, each with a different characteristic strength and temperature domain. Scattering mechanisms in bulk GaAs still affect two-dimensional transport and should be considered.

When multiple scattering effects are present in a system, it is appropriate to use Matthiessen's rule to determine their net effect. The inverse of the total mobility in a material is equal to the sum of the inverses of the individual mobilities due to each scattering effect.

$$\frac{1}{\mu} = \frac{1}{\mu_{\text{impurities}}} + \frac{1}{\mu_{\text{lattice}}} + \frac{1}{\mu_{\text{phonon}}} + \cdots \qquad \text{Equation 1.2}$$

This is an approximation, as it is not valid when scattering effects are dependent on each other. The rule can also be applied to finding the total scattering times and scattering lengths of materials as a result of many different mechanisms.

Some of the most dominant transport scattering mechanisms will be discussed here, first for bulk GaAs. Impurity scattering can be caused by neutral impurities found in imperfect crystals. These may unintentionally be present in GaAs as a result of the growth process are sometimes unavoidable. Neutral impurity scattering typically results in small scattering corrections at low temperatures and is typically considered negligible when compared to ionized impurity scattering. Ionized impurities in the sample are charged,

which results in a much larger scattering cross section. When impurities are charged with potentials comparable to the Fermi energy, this situation creates an effect known as ionized impurity scattering. Both impurity scattering mechanisms can be reduced by improving the crystal growth process.

Electron-phonon scattering is another bulk scattering process found in all materials. Phonons are quasi-particles of lattice vibrations, and are normally thought of as modes of vibrations brought upon through heat in the crystal. In a perfect crystal, only electron-phonon scattering would be present, and reducing the temperature of the material always reduces the scattering from electron-phonon coupling. The electron mean free path is disrupted by lattice vibrations, which can limit their mobility. A characteristic temperature, the Bloch-Gruneisen temperature, is useful to characterize the temperature at which electron-phonon scattering dominates electronic transport. Above the Bloch-Gruneisen temperature, many phonon modes exist, which cause large angle scattering events with electrons. Below this temperature, only phonons with lower momentum than conducting electrons exist, leading to only small angle scattering.

Electron-phonon scattering can take other different forms, especially when lattice vibrations give rise to different physical effects that also cause scattering events. For example, deformation potential scattering is caused by the displacement of atoms from their lattice sites, which results in changes to the band structure. This is one mechanism where electrons are coupled to phonons and can be treated as perturbations of the band energies due to phonons:

lattice vibrations → perturbations of the band energies → electron scattering

GaAs is also a piezoelectric crystal, and exhibits an electric field due to crystal distortions. Lattice vibrations (phonons) can cause minuet crystal distortions, which can scatter charge carriers:

lattice vibrations → piezoelectric effect → electric field → electron scattering

Note that piezoelectric scattering can only occur in compound semiconductors because it needs a polarizable structure. There is no piezoelectric scattering in Si, for example.

Electron-electron scattering is apparent in all electronic systems and is typically unavoidable. This situation comes as a direct result of the Pauli exclusion principle – electrons cannot reside in the same position at the same time. The electron-electron scattering strength varies with the concentration, increasing with increasing electron density. In three dimensions, electrons are generally considered as non-interacting – meaning negligible electron-electron scattering – when the electron density is less than 10^{17} cm^{-3}.

Scattering in two-dimensional systems is more complex, since the electrons' phase space is 2D, while the scattering potentials are still 3D. In two dimensions, impurity scattering can be divided into two considerations: residual donors and remote donors. Residual donors are impurities inside the two-dimensional electron gas. Residual donors have a small effect two-dimensional conduction, since only donors near the 2DEG cause a disorder potential. Remote ionized donors are of extreme significance, since they can contribute to the carrier density and mobility of the two-dimensional conduction. Remote impurities are spatially separated from the electronic conduction, which reduces the strength of their scattering effect. However, the mobility and density of the two-dimensional electron gas is reduced as remote ionized impurities move further from the

conductive plane, as the donor effect weakens. Therefore, a balance can be struck. Place ionized impurities far enough away from the quantum well that they do not create significant scattering and close enough they they donate to the carrier density and therefore the mobility. This technique of taking advantage of remote ionized impurities is known as modulation doping, and is achieved by growing a layer of Si or C approximately 20 nm away from the quantum well in the AlGaAs layer.

Since two-dimensional electronic conduction is almost always realized in a heterointerface of two materials, a significant contribution to electron scattering is due to interface roughness. Imperfections in the interface due to crystal mismatching will create interface roughness, which varies from material to material. In GaAs/AlGaAs quantum wells, the effect is caused by the aluminum in the quantum well. However it has been concluded that the interface roughness scattering strength is insensitive to the aluminum percentage.[10] Since the lattice parameters in GaAs and AlGaAs are so close, this is an extremely small effect in GaAs/AlGaAs heterostructures. Interface roughness is a short range mechanism, understandably so, since it occurs at the conductive interface, and is typically only considerable at low temperatures.

Alloy scattering, another short-range scattering mechanism, may look like interface roughness since both effects are direct results of the presence of aluminum in AlGaAs. The difference between alloy scattering and interface roughness is treated the same theoretically, but the mechanisms are very different physically. Alloy scattering is unavoidable in GaAs and is due to the periodic coulomb potential created by alternating cations (Ga) and anions (As). Again, this form of scattering is small and often negligible in GaAs/AlGaAs quantum wells, though increasing the effective mass, carrier density, and

aluminum concentration will increase the effect. Alloy scattering is much stronger than interface roughness scattering in GaAs/AlGaAs systems.[11] This is thoroughly discussed later in Chapter 3.

It's very easy to become overwhelmed by the terminology and theoretical handling of the many types of scattering mechanisms in two-dimensional systems. This discussion has only skimmed the surface of electronic transport mobility limitations, and is intended to give the reader a qualitative understanding of the most popular and dominant effects in GaAs quantum wells. To summarize, scattering mechanisms are typically split into two categories – long-range scattering (remote ionized impurities, electron-phonon scattering) and short-range scattering (interface roughness and alloy disorder) – though electron-electron scattering can fall into either category depending on the carrier density. At high temperatures (above the Bloch-Gruneisen temperature), electron-phonon scattering dominates. Below the Bloch-Gruneisen temperature, phonon modes with low momenta exist, so electronic scattering effects dominate the mobility.

1.2b $LaAlO_3/SrTiO_3$ heterointerfaces

The discovery of n-type, quasi-two-dimensional electronic conduction at $LaAlO_3/SrTiO_3$ heterointerfaces was made in 2004 by Ohtomo and Hwang.[9] When a thin film of lanthanum aluminate is deposited on a strontium titanate substrate, a quasi-two-dimensional metallic state can be observed. Since their famous publication, many condensed matter and materials science researchers shifted their focus toward materials of this type ($ABX_3/SrTiO_3$). What about this system intrigued so many scientists?

$SrTiO_3$ is an oxide with a perovskite structure, as illustrated in Figure 1.3a. The perovskite structure (ABX_3) has cubic symmetry, where the X anion bonds both A and B

cations. Strontium titanate can be found in nature, but is typically grown artificially in labs using chemical vapor deposition (CVD) processes. It is used in optics, electronics, and jewelry as a diamond alternative. $SrTiO_3$ is an electrical insulator unless doped with niobium or oxygen vacancies, which provide donor charge carriers. Oxygen vacancies are very common in perovskite oxides, since the bonding of oxygen is weak in the perovskite structure. In addition, oxygen atoms form an octahedron that may rotate at low temperatures, reducing the symmetry of the crystal. Growth temperatures and post-annealing can both introduce and strip the material of oxygen atoms, thereby reducing or increasing the number of free charge carriers in the material.

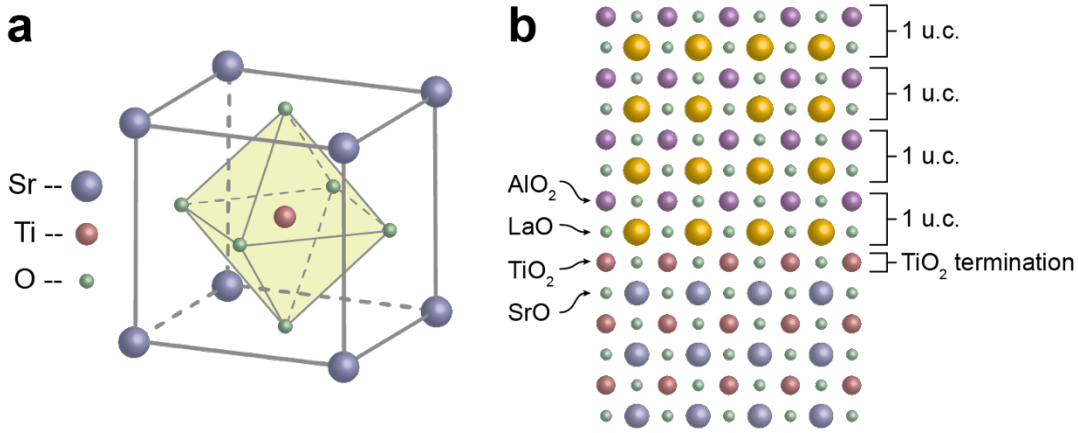

Figure 1.3. (a) Perovskite unit cell of strontium titanate. An octahedron of oxygen atoms occupies the face centers of the cubic crystal formed by strontium atoms. (b) Cross sectional slice of a 4 unit cell (u.c.) lanthanum aluminate/strontium titanate heterointerface. The junction must be TiO_2-terminated $SrTiO_3$.

Lanthanum aluminate, $LaAlO_3$, is a similar inorganic compound with a perovskite structure. It can also be grown epitaxially with CVD methods and is an electrical insulator as well. Metallic behavior is not usually expected when combining two electrical insulators. Insulator + Insulator ≠ Conductor (in most cases). A deeper understanding of heterointerfaces is needed to comprehend and explain the unexpected interfacial

conduction. The following discussion will focus on the requirements for conductivity in $LaAlO_3/SrTiO_3$ heterointerfaces.

Electrical conduction does not occur in lanthanum aluminate/strontium titanate systems unless the $LaAlO_3$ layer is four or more unit cells thick (Figure 1.3b). The explanation for this is simple: to avoid a diverging, runaway electrostatic surface potential, a charge of $e/2$ per unit cell is transferred from the surface to the interface. This electronic reconstruction is energetically favorable in systems with four or more $LaAlO_3$ layers and stabilizes the surface potential. As is, $LaAlO_3/SrTiO_3$ does not have enough free charge carriers to electrically conduct, and this electronic reconstruction is one of a few sources of free carriers. This effect is otherwise known as a polar catastrophe (or an avoidance of it), and can contribute a carrier density of 3.5×10^{14} cm^{-2}, giving a lower limit to the free carrier density of $LaAlO_3/SrTiO_3$ systems. However, carrier densities of higher and lower values than this intrinsic value have been observed, so this phenomenon cannot be the only source of free carriers.

Another contribution to the free charge carriers in $LaAlO_3/SrTiO_3$ systems is the presence of oxygen vacancies. When an oxygen atom is present in the system, it is covalently bonded to the crystal. However, the missing local covalent bond that exists due to a vacant oxygen site results in more free carriers at the interface.[12] Oxygen vacancies in TiO_2 layers of $SrTiO_3$ are also known to release extra *3d* electrons to the quasi-two-dimensional conduction at the interface.[12] In addition, orbital reconstruction depends on the clustering of oxygen vacancies. Evidence for this source of free carriers can be clearly seen by annealing the heterointerface in an oxygen-rich atmosphere. Details of this

procedure are available in Chapter 2. By annealing in oxygen, the number of vacancies is reduced:

annealing in O → less O vacancies → more covalent bonds → less charge carriers

decreasing the carrier density. The opposite effect can be achieved by annealing in a hydrogen-rich environment, where hydrogen atoms bond to weakly bonded oxygen atoms, stripping them from the material. In fact, post-annealing of $LaAlO_3/SrTiO_3$ heterointerfaces have led to carrier densities of less than 1×10^{13} cm^{-2}, far lower than the minimum given by the polar catastrophe picture, which may be explained through the localization of free charge carriers. It can be reasoned that both oxygen vacancies and electronic reconstruction contribute to the free charge carriers responsible for the quasi-two-dimensional conduction at the interface of $LaAlO_3/SrTiO_3$.

In addition, the oxygen growth pressure greatly affects the free charge carriers in $LaAlO_3/SrTiO_3$ systems.[13] Lower oxygen growth pressures give rise to more oxygen vacancies, and can even lead to three-dimensional conduction.[9,14,15] This shouldn't be a surprise considering that bulk strontium titanate conducts with enough oxygen deficiencies. Special attention must be paid to this effect, since it can lead to the overestimation of carrier densities at the interface.

1.2c γ-$Al_2O_3/SrTiO_3$ heterointerfaces

Although $LaAlO_3/SrTiO_3$ is the most popular perovskite oxide heterointerface, numerous materials using $SrTiO_3$ show similar quasi-two-dimensional conductivity. One material in particular is the interface of γ-alumina and strontium titanate. Using molecular beam epitaxy and atomic layer deposition, well-ordered gamma phase aluminum oxide is grown on clean, TiO_2-terminated strontium titanate [001] surfaces, creating γ-$Al_2O_3/SrTiO_3$

that shows conductive behavior at the interface. There are countless similarities to lanthanum aluminate/strontium titanate: carrier concentration on oxygen vacancies, Ti^{3+} signal associated with n-type carriers, requirements of a TiO_2-terminated interface, quasi-two-dimensional interfacial conductivity, moderately high electron mobility at low temperatures (3,000 cm^2/Vs), and conductivity dependent on the Al_2O_3 layer thickness.

Studying γ-$Al_2O_3/SrTiO_3$ interfaces, in addition to $LaAlO_3/SrTiO_3$ interfaces, gives an additional opportunity to study the intrinsic origin of the interfacial conductivity in TiO_2-terminated perovskite oxide heterointerfaces. The common thread between the two systems is strontium titanate, which suggests its role in creating conductive interfaces with perovskite oxides.

1.3 Structural phase transition in $SrTiO_3$

Phase transitions are everywhere in nature. The melting of a Wigner crystal of electrons to an electron liquid or gas is a famous example in condensed matter physics. Phase transitions of electronic states come with added complexities not typically found in phase transitions (inter-particle interaction, direct relation to transport phenomena, screening effects, etc.). Structural phase transitions of crystals are much more straightforward since they lack the complex fluidic motion that liquids exhibit. Strontium titanate, a perovskite oxide band-insulator, undergoes many crystal phase transitions throughout its solid phase. As $SrTiO_3$ is used as a substrate for many heterointerfaces, understanding the effect of the phase transitions on electronic transport is of crucial importance, especially considering that electronic conduction in $SrTiO_3$ heterointerfaces takes place in the Ti^{3+} orbitals.[16]

1.3a Structural phase transitions in two dimensions

Phase transitions can be driven by many different parameters: pressure, temperature, magnetic field, strain, etc. It is a general fact that when a system undergoes a phase transition, it undergoes a change in symmetry. In addition, if the driving parameter in the phase transition is temperature, the higher temperature phase generally has more symmetry than the lower temperature phase (more disorder). Consider the following example.

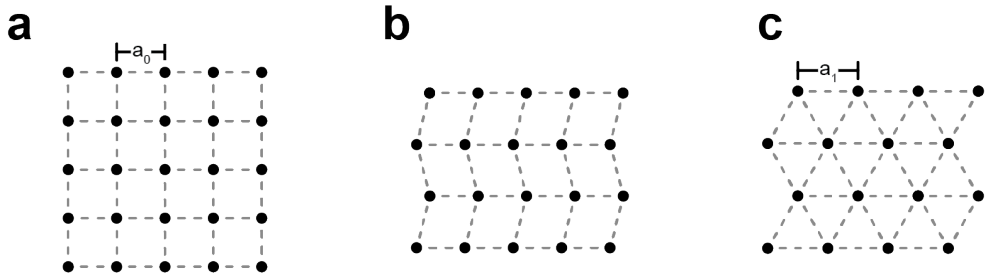

Figure 1.4. Lattice spacing for a two-dimensional cubic lattice as it transitions to tetragonal. At temperature $T > T_c$, the crystal structure is square (a) with a lattice constant of a_0. As the temperature is lowered, buckling occurs (b) and the lattice spacing is reduced, $a < a_0$. The temperature is lowered past the critical temperature, $T < T_c$, below which the crystal transitions into a triangular structure with a spacing of a_1.

Above a critical temperature, T_c, a two-dimensional square lattice of atoms has an atomic spacing of a_0, as depicted in Figure 1.4a. At higher temperatures, a square lattice is energetically favorable. As the temperature is lowered, that energy landscape will transition to favor a triangular crystal lattice and the square lattice undergoes a shear instability. During the transition, an intermediate, metastable buckling phase arises (Figure 1.4b), which is made of alternating parallelograms. This oblique lattice gives way to a triangular lattice at lower temperatures, as seen in Figure 1.4c.[17] Though this is an extremely simple example, and many details (energy landscape, interaction energy, etc.) are glossed over, it

illustrates a very common phenomena found in nature – structural phase transitions. Most of nature can be thought of as phase transitions.

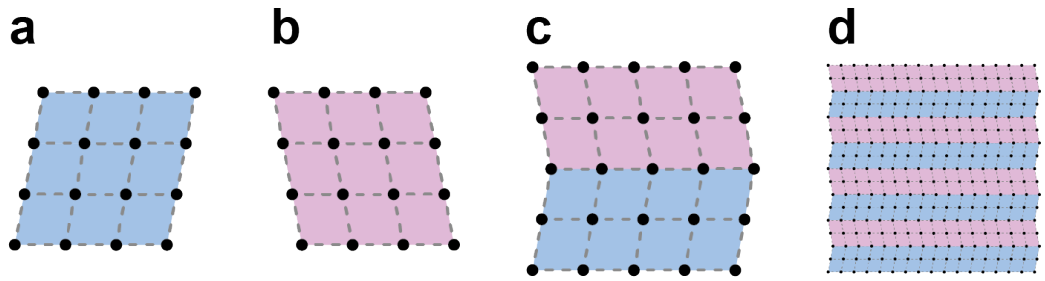

Figure 1.5. (a) Two-dimensional oblique phase with domain D_1. (b) Two-dimensional oblique phase with domain D_2. (c) Tiling rule for domains D_1 and D_2 in the oblique crystal phase. The intersection of crystal domains form a domain wall based on tiling rules. (d) A striped phase of domains D_1 and D_2 forms, resembling a buckling phase.

Figure 1.5a and 1.5c are lattices with a uniform crystallographic domain – the same unit cell repeats over and over. Regions where the same unit cell tessellates without interruption is referred to as crystal domain. To illustrate this concept, consider an oblique lattice with two different crystal domains, Figure 1.5a&b, and note that this discussion is strictly qualitative. Coming from a square phase, the crystal's "choice" of domain may be seemingly random, but depends on a myriad of variables affecting the internal energy landscape of the material. Examples include interstitial impurities, lattice mismatches, atomic vacancies, substitution impurities, and self-interstitial atoms. Internal and external strain, pressure, and external magnetic and electrical fields can also have major impacts on the domain orientation of a crystal.

Regardless of the cause, crystal domains are "chosen" in a material after a phase transition. When the material is much larger than the atomic spacing, it becomes likely that different domains will form in different areas of the crystal, which will inevitably meet. A

domain wall occurs where regions of different crystal domains intersect, as illustrated in Figure 1.5c. Crystal domain walls are a deep, complicated subject matter in both physics and materials science, which could fill several dissertations. For the purposes of this dissertation, only twin domain walls will be discussed. Luckily enough, a twin boundary is the domain wall illustrated in Figure 1.5c. Twin boundaries have a high degree of symmetry and are mirror images of each other across the plain or axis of the boundary.

In certain systems, such as the buckling phase in the two-dimensional square to triangular phase transition, regions of striped order are energetically favorable. Alternating stripes of different crystal domains D_1 and D_2 are also illustrated in Figure 1.5d. In a semiconducting material, such phases can give rise to interesting transport phenomena. At first glance, one may expect a difference in resistivity when current flow is parallel or perpendicular to striped domains. Due to the high degree of symmetry at the domain walls, charge accumulation or deficit may occur at the boundaries. Ferroelectric effects, internal strain, magnetization, and other phenomena due to striped domain walls are not unheard of. Although a two-dimensional example has been used to illustrate these concepts, most materials studied experimentally are thicker than an atom, and the concepts introduced here can be easily extended to a three-dimensional picture.

1.3b Cubic-to-tetragonal phase transition in $SrTiO_3$

In fact, strontium titanate exhibits all of these features. At room temperature (300 K), $SrTiO_3$ has a cubic, perovskite structure (Figure 1.6a). At lower temperatures (105 K*), the crystal transitions to a tetragonal crystal, extending one axis of the unit cell in either the

* The exact temperature is up for debate. See Chapter 5 for more discussion.

[100], [010], or [001] direction. This second-order phase transition is generally assumed to be caused by rotations of TiO_6 octahedra, as shown in Figure 1.6b. Therefore, there are three crystal domains in the tetragonal phase, which are well known to form striped domain walls and twin boundaries. These walls are of great interest to the lanthanum aluminate/strontium titanate community, since evidence suggests that they significantly impact the electrical properties of the interfacial conduction.

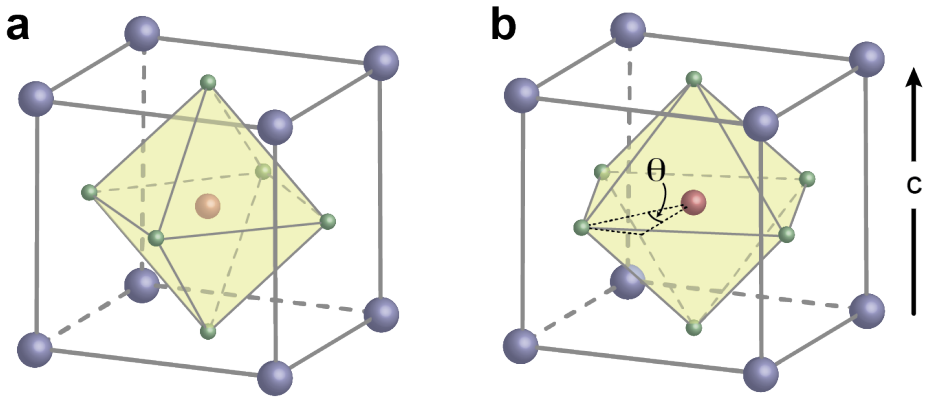

Figure 1.6. (a) Cubic, perovskite structure of strontium titanate at 300K. Blue, green, and red spheres represent strontium, oxygen, and titanium, respectively. Oxygen atoms form an octahedron. (b) In the tetragonal phase, the oxygen octahedra rotate with an angle, θ, and the axis, c, orthogonal to the octahedral rotation extends slightly.

A strain gradient is apparent at strontium titanate domain walls, which causes flexoelectric coupling. Flexoelectricity is found in dielectric materials and results in polarization. It is similar to piezoelectricity, where polarization is due to compressive stress of a dielectric. However, flexoelectricity comes from a rotational stress of a dielectric. Since the dielectric constant is great in strontium titanate – especially at low temperatures – the piezoelectric and flexoelectric coupling at the domain walls, giving rise to a strong polarization across domain walls. In fact, this polarization at twin boundaries has been

calculated to be ~ 0.1-5 $\mu C/cm^2$. This effect is likely to affect electronic transport near domain walls in $SrTiO_3$.[18]

Striped regions of enhanced electrical conductivity and charge accumulation have also been reported due to tetragonal domain walls in lanthanum aluminum/strontium titanate. Local SQUID measurements on the surface of $LaAlO_3/SrTiO_3$ have revealed these anomalies, and raise the question of how else the striped domains may affect electronic transport. Lanthanum aluminate does not have a structural phase transition associated with strontium titanate's cubic-to-tetragonal transition, so the effect is entirely due to the tetragonal domains in the $SrTiO_3$. This makes sense, considering that all electrical transport in $LaAlO_3/SrTiO_3$ systems takes place on the strontium titanate side of the heterointerface. Electrical transport measurements directed at answering these questions are discussed in Chapter 5.

Chapter 2: Samples and experimental setup

2.1 GaAs/$Al_xGa_{1-x}As$ samples

To study scattering mechanisms in GaAs quantum wells at low temperatures, high-quality GaAs quantum wells were grown by John Watson and Michael Manfra at Purdue University. Figure 2.1 shows the layer structure of devices used in this experiment. Samples were grown by molecular beam epitaxy, and were then prepared for measurement. Square samples were prepared with $In_{0.99}Zn_{0.01}$ contacts annealed in a rapid thermal annealer at 450°C for 7 minutes in H_2N_2 forming gas. The contacts were arranged in a Van der Pauw geometry with current applied through two contacts on one side and voltage measured over the opposite side. During annealing, the InZn contacts diffuse through the upper layers of the device to make ohmic contacts with the quantum well (Figure 2.1a&b). The samples had an approximate area of 0.1 cm^2.

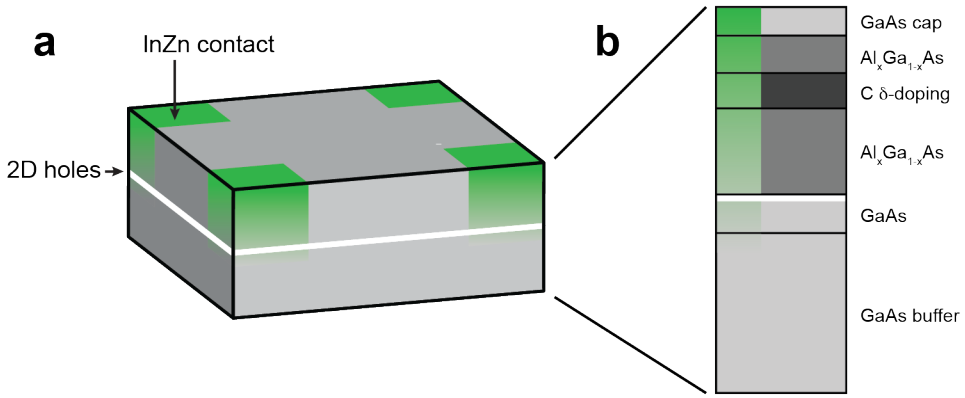

Figure 2.1. (a) Three-dimensional schematic of a typical GaAs quantum well sample. InZn contacts are placed in a square Van der Pauw pattern and annealed deep below the surface. (b) Layer structure for GaAs quantum wells used. Note the InZn contact diffuses through the upper GaAs layers to make a solid electrical connection to the two-dimensional hole gas.

A backgate was applied to the quantum wells by attaching the GaAs sample to a silicon chip with a gold surface. Gold was deposited using a thermal evaporator and worked as the backgate electrode. To increase the efficiency of backgating, the GaAs wafer was sanded down to reduce the distance between the gold backgate and the quantum well. Samples were sanded using progressively finer sandpaper and finished by sanding in a bromine solution, leaving a mirror finish on the back of the sample. Special care must be taken to insure that sanding is uniform and flat, and that the distance (approximately 100 – 500 μm) between the backgate and quantum well is constant. In measurement, the backgates were charged using a direct-voltage power supply up to 10V. The hole density p was lowered by applying a backgate voltage that varied p from 2.23×10^{10} cm^{-2} to 1.09×10^{10} cm^{-2} (corresponding ratio between interhole Coulomb repulsion energy and Fermi energy $r_s = 17 - 25$ using an effective hole mass $m^* = 0.3m_e$, where $r_s = 1/\left(a^*\sqrt{\pi p}\right)$ with p and $a^* = \hbar^2\varepsilon/(m^*e^2)$ being the carrier density and effective Bohr radius where m^*, e, ħ, ε are the effective mass of carriers, electron charge, reduced Planck's constant, and dielectric constant. The samples were measured using lock-in techniques with an excitation current on the order of 1 nA at 7 Hz. With such small heating power ($\sim 10^{-14}$ Watt/cm^2), the samples were cooled to temperatures as low as 50 mK in a ^{3}He/^{4}He dilution refrigerator without overheating the two-dimensional holes by more than a few millikelvins.

2.2 Perovskite oxide samples

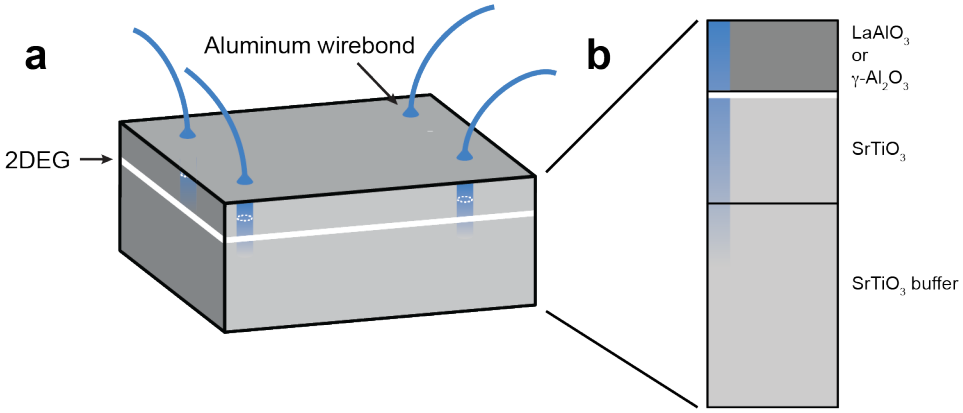

Figure 2.2. (a) Three-dimensional schematic of a typical perovskite oxide heterointerface sample. The schematic is the same for either $LaAlO_3/SrTiO_3$ or gamma-alumina/$SrTiO_3$. Aluminum contacts are wire bonded in a square Van der Pauw pattern, which pierce through the upper oxide to contact the interface. (b) Layer structure for γ-Al_2O_3/ and $LaAlO_3/SrTiO_3$ heterointerfaces used. Note the aluminum wire-bonded contact breaks through the upper layer to make a solid electrical connection to the quasi-two-dimensional electron gas.

Perovskite oxide heterointerfaces are similar to the gallium arsenide samples, as seen in Figure 2.2. Electrical contacts are made through aluminum wire bonding, which breaks through the surface of the top oxide layer to contact the conductive interface. Conduction occurs due to an interface between two materials. Lanthanum aluminate/strontium titanate samples were grown by Dr. Alp Sehirlioglu at Case Western Reserve University using pulsed laser deposition (PLD). Gamma-alumina/strontium titanate samples were grown by Dr. John Ekerdt and Dr. Alexander Demkov at the University of Texas at Austin using atomic layer deposition (ALD). Both samples can be backgated, and special care is taken to make electrical contact with the conducting interface. The differences between lanthanum aluminate and gamma-alumina strontium titanate heterointerfaces are mainly

found in their growth method. However, there are no differences in the methodology used to measure and prepare each sample.

In the instances where backgates were used, nickel was applied to the $SrTiO_3$ substrate using two methods. Nickel paste is a quick, reasonably reliable method of applying a metal backgate. The paste is air-dried for 1 hour, followed by 1 hour of drying on a hot plate at 100C. Higher temperatures and longer times can be used to increase the adhesion of the nickel paste to the sample, although that does not affect the conductivity and reliability of the backgates for the purposes of these experiments. Nickel can also be thermally evaporated using metal deposition techniques. This method is more time and labor intensive, but can lead to a more uniform distribution and adhesion of the nickel to the substrate. Nickel thicknesses of more than 20 nm are adequate.

2.2a γ-Al_2O_3/$SrTiO_3$

Gamma-alumina/strontium titanate samples discussed in Chapter 4 were grown by John Ortmann, Alexander Demkov, Thong Ngo, John Ekerdt, Kristy Kormondy and Bryce Edmondson using molecular beam epitaxy (MBE) and atomic layer deposition (ALD). Using MBE and ALD, films of γ-Al_2O_3 were deposited on TiO_2-terminated $SrTiO_3$ [001] single crystal substrates at temperatures ranging from 200-350 C and 400-800 C, respectively. The thickness of the alumina films ranged from 1.5 nm to 10 nm, though samples discussed in Chapter 4 are 2.1 nm thick.

2.2b $LaAlO_3$/$SrTiO_3$

Lanthanum aluminate /strontium titanate samples discussed in Chapters 4 and 5 were grown by Alp Sehirlioglu and Richard Akrobetu using pulsed laser deposition. $LaAlO_3$ films were deposited on TiO_2-terminated $SrTiO_3$ [001] substrates at 750 C with a partial

oxygen pressure from 10^{-6} Torr to 10^{-4} Torr. Lowering the growth pressure dramatically decreases the oxygen vacancies in the sample, which lend electrons to the conduction band, increasing the carrier density. All samples discussed have $LaAlO_3$ thicknesses of between 6-10 unit cells.

2.3 Micron-scale fabrication of $LaAlO_3/SrTiO_3$

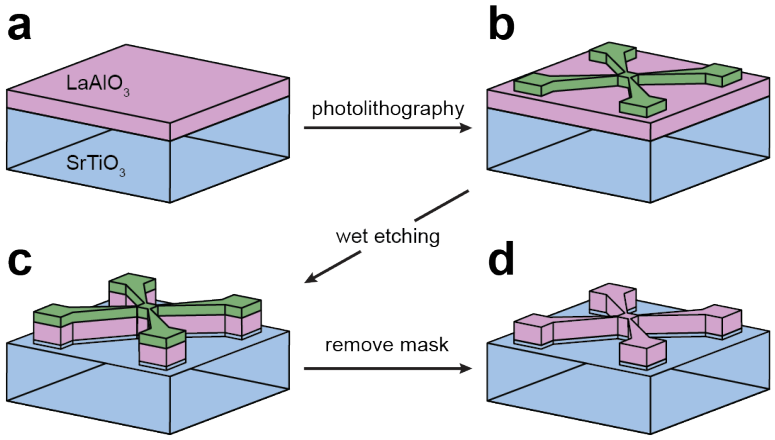

Figure 2.3. Sample reduction process. (a) As-is $LaAlO_3/SrTiO_3$ crystal with a conductive two-dimensional electron gas at the interface. After photolithography, a (b) Van der Pauw photoresist mask remains adhered to the $LaAlO_3$ surface. The unmasked $LaAlO_3$ and underlying $SrTiO_3$ are etched 5-7 nm deep with hydrofluoric acid, removing the two-dimensional conductive interface everywhere except under the Van der Pauw mask. (c) The photoresist mask is removed with acetone, leaving the underlying interface unaffected (d).

Reducing the sample size to the micron scale is necessary to study transport across domain walls, which occur periodically every ~30 μm. Figure 2.3 illustrates the general processing required to reduce the sample size. Photolithograph and wet etching techniques were used to reduce the sample size. Photoresist was spin-coated to the surface of the $LaAlO_3$, which was promptly patterned with a Van der Pauw mask using photolithography. The exposed photoresist was developed, leaving a 100 nm thick pattern of photoresist on

the surface. To increase the stability of the photoresist and selectivity wet etching, the samples were descummed with argon plasma and post-baked for 110°F. Wet etching of the exposed $LaAlO_3/SrTiO_3$ was performed with buffered hydrofluoric acid for 5-7 minutes in order to etch away any interface not covered by the mask. The photoresist was then removed with acetone, revealing a clean, untouched Van der Pattern. Etch depths of at least 6 nm were verified using a Zygo optical profilometer, and electrical contacts were made to verify that no conductive behavior remained on the etched areas.

2.4 Tetragonal domain imaging of $LaAlO_3/SrTiO_3$

In order to image tetragonal domains of $LaAlO_3/SrTiO_3$, samples need to be optically observed under the cubic-to-tetragonal transition temperature. Polarized microscopy is necessary to image domains as well. Linear polarizer filters (catalog #LPVISE2X2) were used as a polarizer and analyzer for polarized transmitted light microscopy. It should be noted that transmission, not reflective light microscopy is necessary to observe tetragonal domain walls most effectively. Samples were placed in a tabletop variable temperature continuous flow SEM microscopy Cryostat with a quartz window (Cryoindustries of America, Inc.) for microscopy use. The samples were imaged as the cryostat was cooled to 77 K using liquid nitrogen. Polarizer and analyzer filters were aligned near 90° in order to reveal the domain walls under 105 K. Multiple temperature cycles on many samples revealed that the domain walls do not rearrange due to thermal cycling. Electrical measurements were taken simultaneously in the microscopy cryostat.

2.5 Low-temperature/low-noise electrical transport measurements

Electrical transport measurements are typical taken using using lock-in amplifiers and 4-wire techniques. This is necessary to reduce experimental error, increase the signal-to-noise ratio, and eliminate any effects from the contacts. In traditional, 2-wire measurements, a known voltage, V_{sample}, is applied to a device under test (DUT), drawing a current, I_{sample}, which is measured with an ammeter. The benefits of this method are found in its simplicity. Only two electrical contacts are needed, and the equipment required is limited to a voltage supply (acting as a current supply) and an ammeter. In situations where equipment is limited or the scale of the DUT is too small to fabricate more than two contacts, a 2-wire measurement is unavoidable. However, this measurement is not ideal. Electrical contacts to a material have an inevitable contact resistance, and this contact resistance is measured along with the DUT resistance using 2-wire techniques. In other words,

$$R_{2-wire} = \frac{V_{sample}}{I_{sample}} = R_{material} + 2R_{contact}, \qquad \text{Equation 2.1}$$

where R_{2-wire} is the measured resistance, $R_{contact}$ is the contact resistance (the factor of 2 reflecting both contacts), and $R_{material}$ is the resistance of the DUT, sometimes referred to as R_{4-wire}, R_{xx}, or R_{xy} depending on the electrical current/voltage configuration.

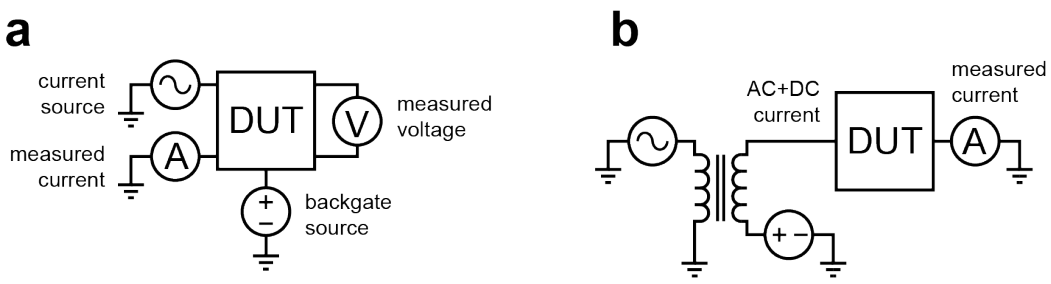

Figure 2.4. (a) Circuit diagram representing a common 4-wire measurement using lock-in techniques. An AC current source is input to the DUT and measured with a lock-in amplifier, while the corresponding AC voltage is measured with a second lock-in amplifier. A backgate can be charged using a DC voltage source. (b) Circuit diagram representing a standard capacitance measurement with a DC offset. A transformer is used to mix AC and DC signals, which is input to the DUT. A lock-in amplifier measures the AC current drawn by the DUT.

Ideally a 4-wire measurement is used to characterize electrical transport in different materials. A typical measurement setup is shown in Figure 2.4a. A lock-in amplifier is used to source an AC electrical current to the DUT, which is measured using a lock-in amplifier resulting in I_{sample}. A corresponding AC voltage is simultaneously measured, giving $V_{material}$. The resulting 4-wire resistance can be calculated using the simple formula,

$$R_{4-wire} = \frac{V_{material}}{I_{sample}}. \qquad \text{Equation 2.2}$$

Both of the terms $V_{material}$ and I_{sample} are affected by the contact resistance, and dividing the two negates the effect. Four-wire resistance is not affected by the contact resistance of the DUT, which allows experimentalists to study inherent properties of materials not subject to contact effects.

Chapter 4 discusses capacitance measurements of strontium titanate. In $SrTiO_3$, the capacitance is affected by the polarization of the crystal, which can be tuned with a backgate. Therefore, capacitance measurements must be completed with a mixed AC+DC signal. The circuit used for this measurement is shown in Figure 2.4b. The AC signal measures the capacitance between the backgate and the two-dimensional electron gas, and the DC signal charges the backgate. Since the dielectric constant of $SrTiO_3$ is large and lock-in amplifiers ignore DC offsets, the mixing of the signals does not alter the AC measurements. A high frequency sign wave (79 Hz at 2 VAC) is mixed with a constant

voltage (-100 VDC to 100 VDC) through use of a transformer. A transformer or alternative mixing component is needed in order to ensure a proper impedance of the sources. The capacitance is then calculated using:

$$I = CV_{max}\omega \sin\left(\omega t + \frac{\pi}{2}\right), \qquad \text{Equation 2.3}$$

where I is the measured current, C is the capacitance in question, V_{max} is the applied AC voltage, and ω is the frequency. Due to the sin factor caused by the phase shift from a capacitor, the measured current is strictly the out-of-phase component.

Low temperature was achieved using a physical property measurement system made by Quantum Design Inc. Samples were mounted on a rotator probe using either nickel paste or cryogenic grease, and lowered in the cryostat. A thermocouple was situated directly below (< 1 mm) the samples and was in good thermal contact with the conductive regions. The temperature changed at a rate of 1 K/s to 20 K/s. In all experiments, all results were independent of the temperature sweep rate.

All electrical connections were confirmed to be Ohmic through exploration of the current/voltage (IV) characteristics of the contacts. If the IV curves of a set of contacts were linear, they were assumed to be Ohmic, and it was therefore appropriate to use AC measurement techniques. If the IV curve was nonlinear, a Schottky barrier or poor physical connection was typically the culprit. Non-Ohmic contacts were corrected by changing the composition of the contact material (the ratio of indium to zinc in GaAs quantum wells), annealing the contacts for a shorter or longer time, or simply making contacts on a different physical location on the sample.

All measurement data was collected using a National Instruments BNC-2090 rack-mounted BNC terminal block. Data was sampled once every 50 ms, and measured

resistances were averaged over every four data points. The NI BNC-2090 was connected to a PC running Windows through a serial connector. LabVIEW 2015 was used to record and analyze all signals measured by the BNC terminal block, which were then saved as .dat files. OriginPro was used to further analyze and plot all data except for Figure 5.6, which was generated using Quickfield, plotted using MATLAB, and colored/designed using Adobe Illustrator. In some cases, custom scripts were written to optimize the analysis process in LabTalk, a scripting language native to Origin.

Chapter 3: Short-range scattering of two-dimensional holes in quantum wells

Understanding the nonmonotonic behavior in the temperature dependent resistance $R(T)$ of strongly correlated two-dimensional carriers in clean semiconductors has been a central issue in the studies of 2D metallic states and metal-insulator transitions. The transport of high mobility 2D holes in 20-nm-wide GaAs/$Al_xGa_{1-x}As$ quantum wells with varying short-range disorder strength has been studied. By changing the Al fraction x in the $Al_xGa_{1-x}As$ barrier, the short-range interface roughness and alloy scattering are varied. It is observed in correlated two-dimensional hole systems with interaction parameters $r_s \sim 20$, that increasing x suppresses both the strength and characteristic temperature scale of the two-dimensional metallicity, pointing to the distinct role of short-range vs long-range disorder in two-dimensional metallic transport.

3.1 Scattering mechanisms and the nonmonotonic resistance peak

For the past 30 years, two-dimensional quantum systems have been a rich area of concentrated study for both theorists and experimentalists to explore the interplay between Coulomb interaction and disorder effects.[19–22] In the case of two-dimensional electrons with ultralow density and weak disorder, the quantum and strongly interacting nature of the systems becomes so prominent that various complex quantum phases and phase transitions may exist according to theory.[23–29] Obtaining a clear understanding of such strongly correlated two-dimensional systems thus remains extremely important in the field of many-body physics.

In two-dimensional electron or hole samples with high mobility, an intriguing metal-to-insulator transition was observed in zero magnetic field ($B = 0$) with the charge carrier density as the tuning parameter.[2,19,22] Although strong electron-electron interactions are believed to be an essential factor in the origin of this metal-insulator transition in two dimensions, the effects of disorder seem to be non-negligible and must be incorporated in order to reconcile the subtle differences in all of the two-dimensional metal-insulator transition experiments over a range of disorder and interaction strength.[19,22,30–32] While the understanding of the two-dimensional metal-insulator transition in the critical regime continues to advance,[30–34] the mechanism of the two-dimensional metallic conduction in the metallic regime (resistivity $\rho \ll h/e^2$) remains an outstanding problem under debate.[21,35] Since metallic transport is the central phenomenon that challenges conventional wisdom based on localization and weakly interacting Fermi liquid theory, its understanding would shed light on the two-dimensional metal-insulator transition and transport of correlated two-dimensional electron fluids in general. After extensive transport studies over the past two decades, a salient feature of two-dimensional metallic transport has now emerged: when measured over a broad temperature range from $T \ll T_F$ to $T \sim T_F$, where T_F is the Fermi temperature, a nonmonotonic behavior is commonly found in the temperature dependent resistivity.[36] Specifically, as phonon scattering is reduced at low temperatures, electron-impurity scattering and electron-electron interactions contribute more to the longitudinal resistance R_{xx}. The electronic contribution to the resistance behaves nonmonotonically, first increasing and then decreasing as T is lowered past a characteristic temperature T_0, which is comparable to T_F. This feature, better observed in low density two-dimensional systems, occurs when charge carriers become semi-degenerate and has

been observed in the three most commonly studied two-dimensional systems: *p*-GaAs,[36–39] *n*-Si,[40,41] and *n*-GaAs.[4,42] The mechanism of this nonmonotonic $R_{xx}(T)$ has been a key point in several leading theories of the 2D metallic transport[23,24,43–45] and is the subject of the following experimental study.

The nonmonotonic temperature dependent transport associated with the metallic transport in a two-dimensional hole system is impacted by short-range disorder scattering. The strength of this impact is studied in a series of modulation doped GaAs/$Al_xGa_{1-x}As$ quantum wells with varying barrier height x. In these quantum wells, it is well known that a change in the aluminum concentration adjusts the short-range disorder potential via two important scattering mechanisms: interface roughness and alloy scattering[10], thus providing an opportunity to systematically investigate the effect of controlled short-range disorder strength on the two-dimensional metallic behavior in similar quantum well or heterointerface systems. Tuning the strength of the short-range disorder potential has a marked impact on both the strength and temperature scale of the nonmonotonic $R_{xx}(T)$. Nevertheless, the overall shape of the $R_{xx}(T)$ does not change in a qualitative manner, exhibiting universality. These findings demonstrate that the nature of disorder (e.g. short-range vs long-range scattering) is an important ingredient in a quantitative understanding of the two-dimensional metallic conduction with resistivity $\rho \ll h/e^2$, as pointed out in a previous report[46] where different types of two-dimensional semiconductor heterointerfaces were analyzed.

3.2 The effect of quantum wall barrier height on electronic transport

The following experiments were performed on high mobility, low density two-dimensional hole systems (2DHS) in 20 nm-wide GaAs asymmetrically doped quantum

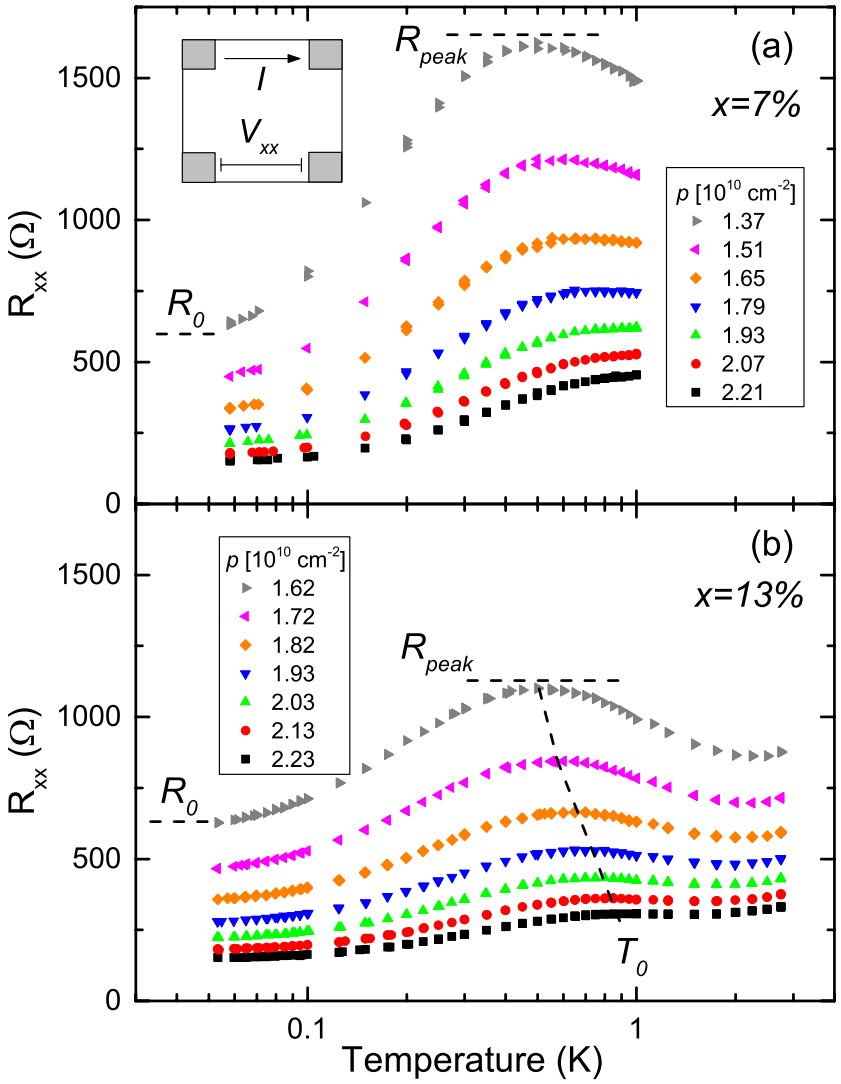

Figure 3.1. Longitudinal resistance R_{xx} vs T of two-dimensional holes in a 20-nm-wide GaAs/$Al_xGa_{1-x}As$ quantum well with aluminum mole fractions of (a) 7% and (b) 13% in the $Al_xGa_{1-x}As$ barrier. The dotted lines mark T_0, the position of the peak in $R_{xx}(T)$.

wells located 190 nm below the surface.[11] The samples were grown in the [001] direction using molecular beam epitaxy (MBE). The short range disorder potential was varied by controlling the aluminum mole fraction x in the $Al_xGa_{1-x}As$ barrier. Measured x's were 0.07 (7%), 0.10 (10%), and 0.13 (13%) with δ-doping setback distances d of 80, 110, and 110

nm, respectively. The ungated samples have hole mobilities of $\mu \approx 0.5 - 1.0 \times 10^6$ cm^2/Vs. Square samples were prepared with InZn contacts in a Van der Pauw geometry as described in Chapter 2.1 and the schematic inset in Figure 3.1.

3.3 Longitudinal resistance in the Bloch-Gruneisen regime

Figure 3.1 shows the raw $R_{xx}(T)$ data for a sample with (a) 7% and (b) 13% aluminum mole fractions in the barriers. Longitudinal resistance was measured from low temperatures $T \sim 50$ mK up to high temperatures $T = 1 - 4$ K. Varying the carrier density predictably changes the nonmonotonic behavior by proportionally shifting the characteristic temperature T_0, at which $(dR_{xx})/dT = 0$. This defines the position of the nonmonotonic peak of interest. Similar to previous experiments,[37] T_0 becomes higher when the hole density increases. It has been shown that the temperature dependence of R_{xx} on the metallic side of the metal-insulator transition follows[36]

$$R_{xx}(T) = R_0 + R_{ph}\frac{t^3}{1+t^2} + R_{el}(T), \qquad \text{Equation 3.1}$$

where R_0 is the residual resistance as $T \to 0$, R_{ph} is the Bloch-Gruneisen resistance, $t \equiv T/T_{ph}$, T_{ph} is the Bloch-Gruneisen temperature, and R_{el} is the T-dependent part of the electric contribution to R_{xx}, which can be fit to the empirical form[36]

$$R_{el}(T) = R_a x^{-1}(\alpha + x^{-2})^{-\frac{1}{2}}\exp(-x^{-1}), \qquad \text{Equation 3.2}$$

where $x = kT/E_a$, E_a is the activation energy and is proportional to T_0, and α is a constant. As seen in Figure 3.1b, at temperatures higher than ~2 K, $R_{xx}(T)$ increases with T. This is due to the phonon scattering term dominating over the electronic term above

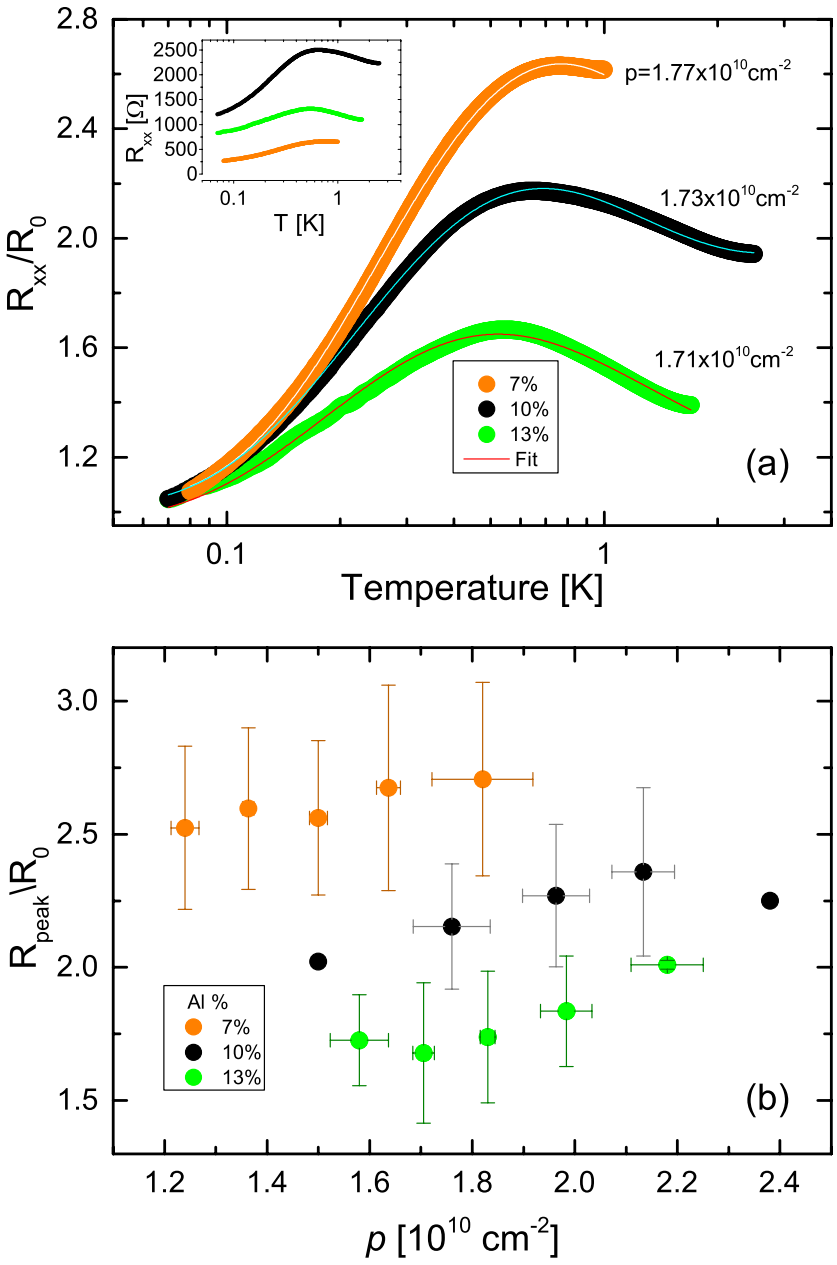

Figure 3.2. (a) The temperature dependent resistance, normalized with R_0, for 20-nm-wide GaAs/Al_xGa_{1-x}As quantum well with 7%, 10%, and 13% aluminum mole fractions at p = 1.77, 1.73, and 1.71 × 10^{10} cm^{-2}, respectively. The model fit of Equation 3.1 is indicated by the solid lines. The inset plots the un-normalized resistance as a function of temperature. (b) Dependence of the strength of the two-dimensional metallicity as defined by the ratio of resistance at the peak of *R(T)* and residual resistance on the hole density. The error bars come from averaging measurements from different current/voltage configurations and different samples. Zero-bias densities are the maximum densities for each Al%.

the Bloch-Gruneisen temperature.[36] At lower temperatures where the phonon term diminishes rapidly (according to $\sim T^3$ power law dependence), the electronic term $R_0 + R_{el}(T)$ shows a nonmonotonic behavior: R_{xx} first rises to $R_{peak} = R_{xx}(T_0)$, the maximal value of R_{xx} at T_0, then drops towards R_0 as T reduces towards zero.

Comparing the $R_{xx}(T)$ curves in Figures 3.1a and 3.1b suggests that the nonmonotonic electronic impurity scattering peak is more pronounced in the sample with 7% aluminum in the barrier. To further elaborate and quantify this, the effect of short-range scattering on the nonmonotonic $R_{xx}(T)$ peak for three different aluminum percentages were studied. Figure 3.2a shows the temperature dependent resistance normalized over R_0 for samples with 7%, 10%, and 13% aluminum in the barrier, respectively. Note that to clearly and reliably illustrate the evolution of the $R_{xx}(T)$ peak against aluminum percentage, curves for similar hole densities (1.71, 1.73, and 1.77×10^{10} cm^{-2}) are presented, and the curve for each aluminum mole fraction was obtained by averaging over different samples and current-voltage contact arrangements as per the Van der Pauw method. Here, R_0 was obtained by fitting the curve to Equation 3.1, and the hole density was obtained by the positions of Subnikov-de Hass oscillations at low T. Figure 3.2a shows that the relative strength of the nonmonotonic $R_{xx}(T)$ peak does become stronger at lower aluminum percentages, although it is harder to identify this effect in the raw $R_{xx}(T)$ data (Figure 3.1a) due to differences in the absolute values of the resistance (or the mobility). Note that to reduce data manipulation, the phonon scattering term was not subtracted from the raw resistance data in Figure 3.1a. However, separating the electronic scattering from the phonon scattering in $R_{xx}(T)$ does not change the curves in any significant way. Briefly, fitting to Equation 3.1 was first conducted to determine how well the data fit the model

described in Ref 36. As shown by the solid lines in Figure 3.2a, the fits agree well with the measured behavior. Using methods discussed by Mills *et al*. in Ref 36, the electronic scattering part is isolated, which does not differ much from Figure 3.1a. In addition, fitted parameters (R_0, R_{ph}, R_a, T_{ph}, and E_a) and the constant ($\alpha = 2.5$ as suggested by Ref 36) from Equations 3.1 and 3.2 were extremely consistent with those in Ref 36. The constant α does not vary significantly between samples with different aluminum concentrations and was kept constant in an effort to reduce fitting parameters. The difference between hand-selecting and fitting R_0 and R_a was insignificant.

Such analysis was conducted across the entire range of hole densities, and R_{peak}/R_0 values were extracted after removing the phonon scattering term. These values were plotted for various different hole densities for the three sets of quantum wells with different aluminum fractions previously mentioned (7%, 10%, and 13%). The results are shown in Figure 3.2b. Averaging over different current-voltage contact configurations and similar hole densities is taken into account through the error bars. Due to imperfect contact alignment and perhaps slight inhomogenaties in the charge carrier density and mobility in the wafers, the metallicity strength parameter, R_{peak}/R_0 varies somewhat between different samples with the same aluminum concentration or current-voltage contact arrangements on the same Van der Pauw sample. However, it is still clear that R_{peak}/R_0 increases from ~1.7 in quantum wells with 13% aluminum in the barrier to ~2.7 in quantum wells with 7% aluminum in the barrier. Therefore, Figure 3.2b demonstrates that the behavior described in Figures 3.1 and 3.2a is true for our entire range of densities: an increase in the aluminum fraction in the barrier suppresses the two-dimensional metallic behavior for high mobility, low density two-dimensional hole systems in GaAs quantum wells.

3.4. Characteristic temperature in response to disorder

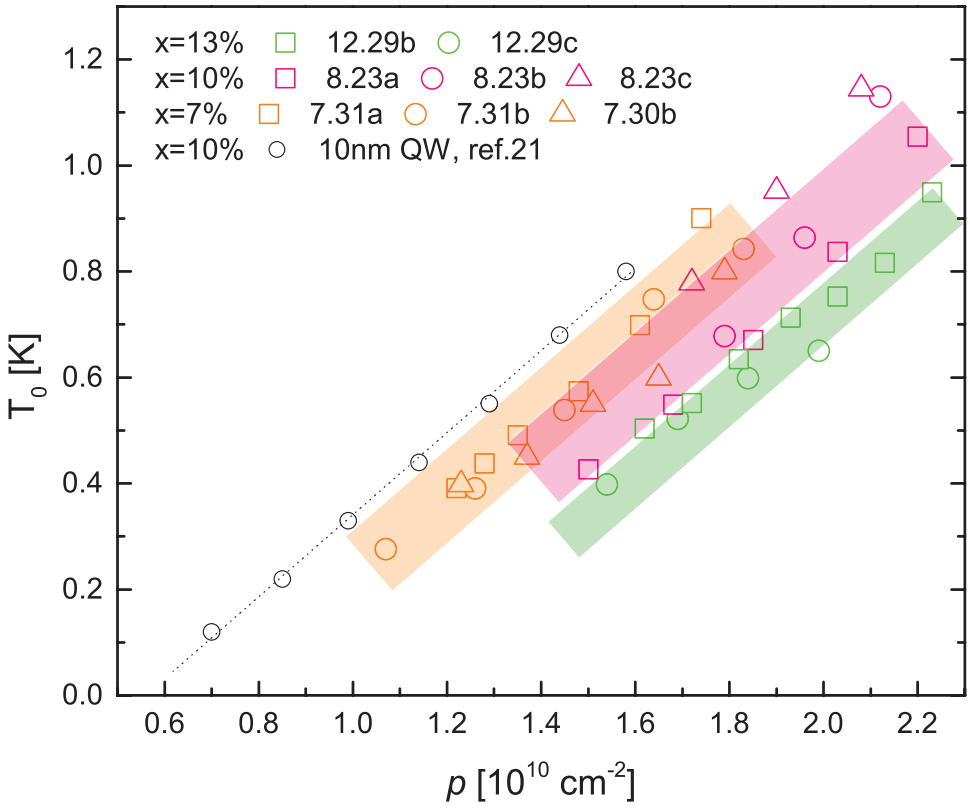

Figure 3.3. Characteristic temperature T_0 vs two-dimensional hole density for various GaAs quantum wells with different aluminum fractions in the barrier, where T_0 represents the temperature at which $R_{xx}(T)$ peaks.

In addition to the strength of the nonmonotonic resistance peak, the position of the peak was studied, depicted by the characteristic temperature T_0, defined as the temperature where $dR_{xx}/dT = 0$. From Figure 3.1, it can be seen that R_{ss} changes its behavior from metallic to insulating-like above T_0. The characteristic temperature becomes larger when p increases, which is consistent with the previous findings in literature.[36,37] Despite the obvious importance of T_0 in any theory about two-dimensional metallic conduction and metal-insulator transitions, it is surprising that there are no systematic experimental investigations on what other parameters besides the charge carrier density (e.g. interaction

strength, mobility) control T_0. Figure 3.3 shows T_0 as a function of hole density for all the $R_{xx}(T)$ measurements. Different markers indicate different samples or different Van der Pauw measurement configurations for the same sample, and shaded areas highlight trends. Similar to the shift in R_{peak}/R_0, a definite trend in T_0 emerges as the aluminum concentration increases in the barrier: higher aluminum concentration leads to a lower T_0. It is also interesting to compare the trend of T_0 in the series of 20-nm-wide quantum wells with a prior study on 10-nm-wide quantum wells grown on [311]A GaAs.[37] Despite that the 10-nm-wide quantum well in Ref 39 had a 10% aluminum concentration in the barrier, it showed a T_0 higher than all of the 20-nm-wide [001] samples studied here, reflecting the importance of having all other structural parameters consistent except changing only one parameter (aluminum percentage). However, it is intriguing that the overall linear trend of T_0 vs p is similar and has almost the same slope between Ref 39 and this study.

3.5 Universality of the electronic contribution and its implications

Figure 3.4 shows the overall shape of the temperature dependent electronic contribution to R_{xx} and is qualitatively unchanged throughout all measurements, regardless of the percentage of aluminum in the barrier. By fitting Equation 3.1 to the raw R_{xx} data, the residual resistance R_0 and the Bloch-Gruneisen coefficients were determined. Using the fitted parameters, the electronic contribution to R_{xx} was calculated by subtracting R_0 and the phonon contributions. To show a universality of the R_{el} peak, this was completed for all aluminum concentrations and various charge carrier densities. For an easier comparison without putting the data in the context of any specific model, the resistance and temperature have been normalized with the height of the electronic contribution peak, $R_{peak} - R_0$, and T_0, respectively. Due to the universality demonstrated, it is clear that the shape of the

electronic contribution is independent of the microscopic details of the short-range disorder potential.

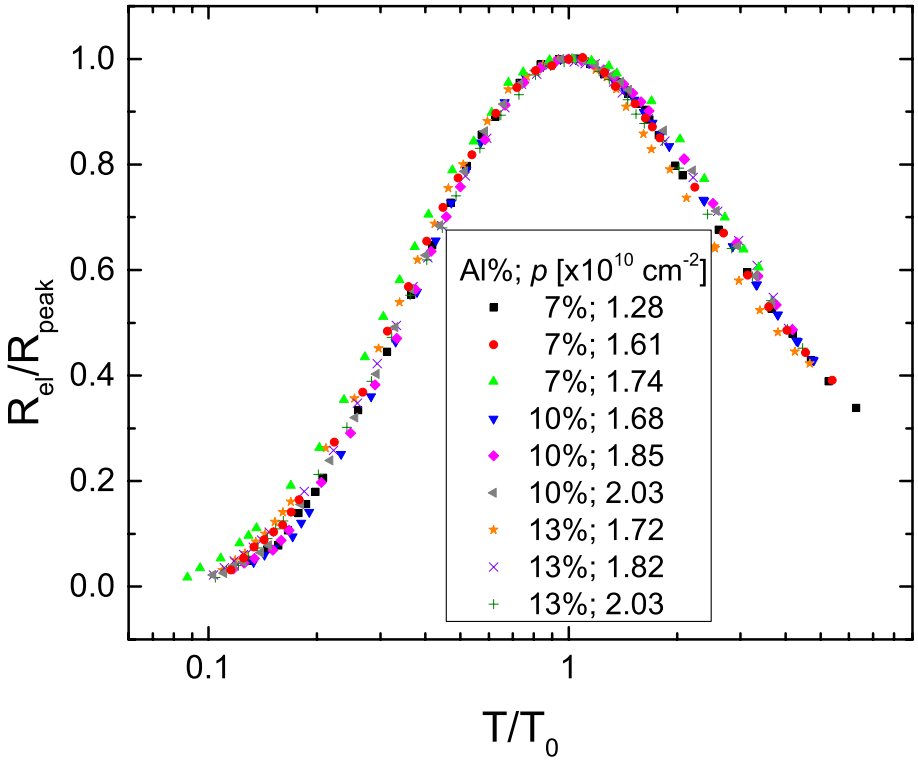

Figure 3.4. The dimensionless, T-dependent part of the electronic contribution to R_{xx}, normalized to the height of the resistance peak in $R_{xx}(T)$, plotted against temperature normalized by the characteristic temperature T_0.

The implications of the experimental observations are now explored. In a previous work, Clarke *et al*. pointed out that it is important to distinguish the short- vs long-range nature of dominant disorders in different semiconductor heterointerface systems to resolve the conflicting metallicity strength.[46] The effect of systematically controlled short-range disorder strength has been studied here from interface roughness and alloy scattering in *p*-GaAs, since all of the samples have the same quantum well width and similar dopant

setback distances. In addition, by performing measurements to high temperatures ($T > T_F$), the universal shape of nonmonotonic $R_{xx}(T)$ in samples exhibiting different low temperature metallic strengths has been observed. To date, the effect of short-range vs long-range (remotely ionized dopants) disorder on the nonmonotonic $R_{xx}(T)$ from the high temperature ($T \sim T_F$) to the low temperature ($T \longrightarrow 0$) regime has not been carefully addressed in relevant theories.[23,24,43–45] Given the consistent and significant impact of short-range scattering on both the quantitative strength (R_{peak} / R_0 differs by almost two times from x = 7% to 13%) and characteristic temperature or energy scale of the two-dimensional metallicity, it now becomes essential to differentiate the nature of disorder in quantitative theories about the metallic transport. Such effects could be readily incorporated and tested in Boltzmann transport-based theories.[45] Within the Fermi liquid interaction correction theory of the metallic transport,[47] it can be argued that stronger short-range disorder promotes large angle back scatterings of particles to interact with themselves, and therefore the metallic correction should be stronger.[46] In a work by Ando,[10] it was concluded that the interface roughness scattering strength is insensitive to the aluminum percentage in GaAs/$Al_xGa_{1-x}As$ heterointerfaces if a constant roughness parameter (typically a few angstroms) is assumed. Meanwhile, the short-range alloy disorder potential in $Al_xGa_{1-x}As$ should be proportional to $x(1-x)$, i.e. increasing function of x in the studied range of $x = 0.07 - 0.13$. However, the alloy disorder scattering rate turns into a decreasing function of x after taking into account the exponentially suppressed carrier wave function within the $Al_xGa_{1-x}As$ barrier as x increases.[10] Therefore, one expects stronger short-range disorder scattering at smaller x values in our samples within the single particle relaxation model, and our finding of a stronger metallic resistivity drop at lower x agrees with Ref 46. Note

that the condition of $k_b T_F \gg k_b T > \hbar/\tau$ required in the Fermi liquid interaction theory in the ballistic regime[47] is not met in this experiment when the metallic conduction occurs, and the Hall coefficient in high mobility *p*-GaAs quantum wells shows anomalous behavior as compared to the Fermi liquid interaction theory. For instance, $(\hbar/\tau)/k_b$ is estimated to be ~0.2 K for $p\sim1.5$ in Figure 3.1, where the resistivity ρ is calculated from R_{xx} as $\rho = \pi R_{xx}/\ln 2$ according to the Van der Pauw method. Thus it would be inappropriate to attempt to further quantify the Fermi liquid parameter F_0^σ by fitting the data to theory.

In the literature, it is well understood that the mobility of high quality two-dimensional carriers in modulation doped heterostructures is limited by long-range disorder scatterings such as remote ionized impurities or ionized background impurities[11] but not the interface roughness or alloy scattering[10] in the low density regime. In the samples studied here, a decreasing trend of mobility (in the $T \longrightarrow 0$ limit) is observed when the samples were gated to lower charge carrier densities (Figure 3.5), indicating the dominance of long-range Coulomb scattering as opposed to short-range disorder scattering in the low temperature mobility. It is thus striking to see that short-range disorder plays a clear role in setting the magnitude of the nonmonotonic $R_{xx}(T)$ peak in dilute two-dimensional carrier systems when the system is cooled down from $T\sim T_F$ to $T \ll T_F$.

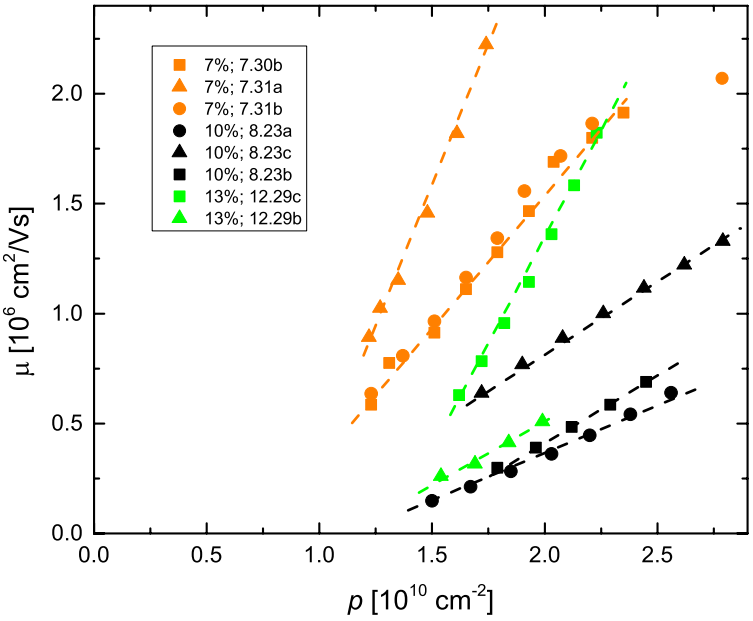

Figure 3.5. Low temperature ($T \longrightarrow 0$) mobility as a function of backgate-controlled hole density in 20-nm-wide GaAs quantum wells with different aluminum mole fractions in the $Al_xGa_{1-x}As$ barrier. Different symbol colors correspond to different x in the $Al_xGa_{1-x}As$ barrier (orange: x = 7%; black: x = 10%; green: x = 13%), and different symbol shapes correspond to different samples or current-voltage configurations. The dashed lines are a guide to the eye.

The systematic shift of T_0 to higher scales in quantum wells with lower aluminum mole fractions is intriguing. In all the theories invoking a nonmonotonic $R_{xx}(T)$ peak in the metallic regime,[23,24,43–45] the crossover temperature T_0 is controlled by the Fermi temperature T_F, which is indeed linearly proportional to the density p in two dimensions and is comparable to the values of T_0 found in experiments. The observation of $T_0 \propto p - p_c$ in Figure 3.3 where p_c is controlled by the disorder strength/type is more consistent with a two-component picture of the two-dimensional metallic state involving a mobile component with a density $p - p_c$ and more localized part with density p_c.[48] In such a perspective, T_0 should be controlled by the Fermi temperature of the mobile component

and thus naturally explains the appearance of the offset by p_c in the linear proportionality between T_0 and p. Since the studied systems reside in the low disorder regime [resistivity as low as $\sim (h/e^2)/50$, has strong correlations ($r_x \sim 20$), and has a suppressed Hall response,[48,49] it is tempting to speculate that the localized component in the two-dimensional metallic state arises from bubbles of a Wigner crystal in a Fermi liquid background.[21,23,24] How the viscosity of such a microemulsion phase of electron crystal and fluid depends on the disorder type would be an interesting theoretical issue[50] to compare with this experiment. A recent two-component semi-classical effective medium theory for the two-dimensional metallic state may also be consistent with this speculation.[51] A systematic and quantitative investigation of the crossover temperature T_0 and R_{peak}/R_0 vs short-range disorder strength and charge carrier density in such a theory would be desirable.

Chapter 4: Metal-insulator transition in perovskite oxide heterointerfaces

Chapter 3 discussed work involving scattering mechanisms in metallic states of two-dimensional electron gasses in GaAs quantum wells. Perovskite oxide heterointerfaces are a new class of material exhibiting quasi-two-dimensional conductivity. Since GaAs quantum wells have been studied for over 35 years, the collection of research on the material is astounding and frankly overwhelming. Novel research on intrinsic behavior related to the composition or growth of GaAs quantum wells is more difficult to achieve; most of the characterization of the system has been understood for many years. In order to provide new insight, experimentation must narrow its focus, filling in gaps that more general research has left untested. Nowadays, GaAs quantum wells are mainly used to study novel phenomena only observable in such high mobility systems, such as the 5/2 fractional quantum Hall state,[52] the anomalous Hall effect,[53] spin coherence, and particle braiding[54] to name a few. Alternatively, perovskite oxide heterointerfaces are a more adolescent class of two-dimensional materials. Discovered in 2004,[9] $LaAlO_3/SrTiO_3$ was the first realization of a conductive interface between two oxide materials. Its demonstration of superconductivity,[55] giant in-plane magnetoresistance,[56] and persistent photoconductivity[57] only increases its intrigue. With its relatively new status in condensed matter physics comes a need for electrical characterization, unlike the already established GaAs quantum well. Since the metal-to-insulator transition was such a highly controversial topic at the dawn of two-dimensional electronic systems, observing the behavior in

perovskite oxides seems to be a natural first step in characterizing their electronic properties.

4.1 Strontium titanate in an electric field

A metal-to-insulator transition is possible in perovskite oxide heterointerfaces. The transition has been shown to exist in $LaAlO_3/SrTiO_3$ heterointerfaces through backgate control,[58] electrolyte topgating,[59] and charge writing.[60] So far, however, metal-to-insulator transitions in other perovskite oxide interfaces, such as γ-$Al_2O_3/SrTiO_3$, have not been investigated. This is surprising considering that $LaAlO_3/SrTiO_3$ is just one of an extensive list of conductive interfaces with strontium titanate as a substrate: $CaZrO_3/SrTiO_3$,[61] $KTaO_3/SrTiO_3$,[62] $DyScO_3/SrTiO_3$,[63] $La_{0.5}Al_{0.5}Sr_{0.5}Ti_{0.5}O_3/SrTiO_3$,[64] amorphous-$YAlO_3/SrTiO_3$,[65] amorphous-$LaAlO_3/SrTiO_3$,[65] γ-$Al_2O_3/SrTiO_3$,[66] $NdGaO_3/SrTiO_3$,[67] $NdAlO_3/SrTiO_3$,[67] $PrAlO_3/SrTiO_3$,[67] $LaGaO_3/SrTiO_3$,[68] $LaVO_3/SrTiO_3$,[69] $LaTiO_3/SrTiO_3$,[69] and $GdTiO_3/SrTiO_3$.[70] Observing the metal-to-insulator transition in new two-dimensional materials not only strengthens the case for a two-dimensional metallic state, it provides a chance of detecting new physical phenomenon and characterizing the tunability of electronic transport each system. Every system is unique and has its own intricacies; understanding those intricacies gives researchers better tools and evidence with which to predict electronic transport in future materials.

In any system, a metal-to-insulator transition via gate effect is encouraging, since it can very easily lead to transistor-like switching behavior of MOSFETs. Strontium titanate is obviously crucial to the formation of a quasi-two-dimensional electron gas at a perovskite oxide heterointerface. This is because conduction occurs in the Ti 3*d* orbitals of the TiO_2-terminated $SrTiO_3$ at the interface, and electronic reconstruction in avoidance of

a polar catastrophe gives rise to those conductive orbitals. With this in mind, there are many motivations to study the metal-to-insulator transition through back gating of the device, as opposed to top gating. Since the polar catastrophe model is sensitive to the surface charge of the material ($LaAlO_3$ or γ-Al_2O_3 for example), the addition of a metallic top gate can significantly affect the electronic reconstruction and therefore the interfacial conduction band. Surface charge writing, which is done with a charged atomic force microscope tip, is a unique procedure, albeit slow, small scale, and impractical. In terms of engineering a gateable perovskite oxide heterointerface, back gating wins in terms of simplicity and effectiveness. A conductive paste on the back surface of the device can generate electric fields capable of inducing a metal-to-insulator transition in $SrTiO_3$ heterointerfaces.

How does strontium titanate behave in an electric field? Most prominently, the $SrTiO_3$ crystal becomes polarized. The dielectric constant at 300 K is quite large, $\varepsilon_r = 300$, and increases as the temperature is lowered, as shown in Figure 4.1. Between ~100 K and ~250 K, the dielectric constant follows the Curie-Weiss law, diverging from the law at the cubic-to-tetragonal structural phase transition.[71] At temperatures below 10 K, ε_r can reach values above 10^4, making it a good candidate for a dielectric medium in capacitor applications. However, the dielectric constant of $SrTiO_3$ changes in an applied electric field similar to its change with temperature. At temperatures below 65 K, ε_r becomes strongly dependent on the electric field (i.e. back gate), decreasing over an order of magnitude from 10 V/cm to 23000 V/cm (Figure 4.1). This result is most likely enhanced due to the orthorhombic crystal phase of strontium titanate at 65 K.

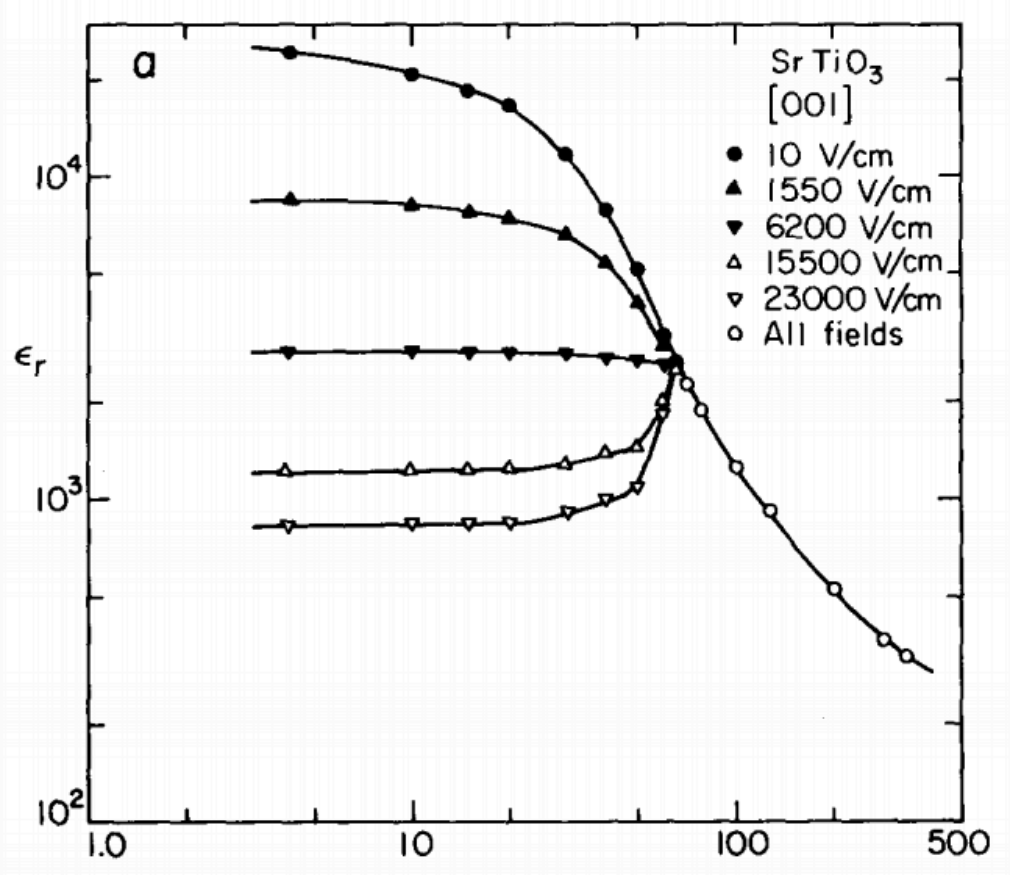

Figure 4.1. Temperature dependence of the dielectric constant of strontium titanate [001] in electric fields applied with a back gate. Electric field dependence is greatly enhanced below 65 K. Reprinted from "Permittivity of strontium titanate." By R. C. Neville, B. Hoeneisen, and C. A. Mead, *Journal of Applied Physics* 45(5), 2124-2131 (1972).

An electric field in $SrTiO_3$ can affect more than the dielectric constant. These additional effects, however, have either minor impacts on electrical transport or should only be considered in very specific instances. For example, tetragonal domains are known to form striped regions of enhanced conductivity and charge carrier density below 105 K. Applying large electric fields via backgating can essentially erase the striped domain boundaries, thereby affecting anisotropic transport on a local scale.[72,73] In addition, backgating can bend the conduction band at the interface, releasing electrons trapped

through the persistent photoconductivity effect.[57] These effects, although minimal, can cause dramatic changes in the electrical transport under the right conditions.

4.2 Gating effects on STO

Since the back gate on a perovskite oxide heterointerface depends on the charging effect through strontium titanate, it is crucial to consider all possible effects from the electric field. In essence, the strontium titanate acts as a parallel plate capacitor with a dielectric constant varying with temperature and the electric field. If ε_r is known, a simple parallel plate capacitor model can be used to calculate the expected change in carrier density at the interface. Since the theoretical description of the dielectric constant of strontium titanate is not accurate enough to predict the experimental value of measured samples, ε_r is extracted from capacitance measurements between the back gate and conductive interface of γ-$Al_2O_3/SrTiO_3$.

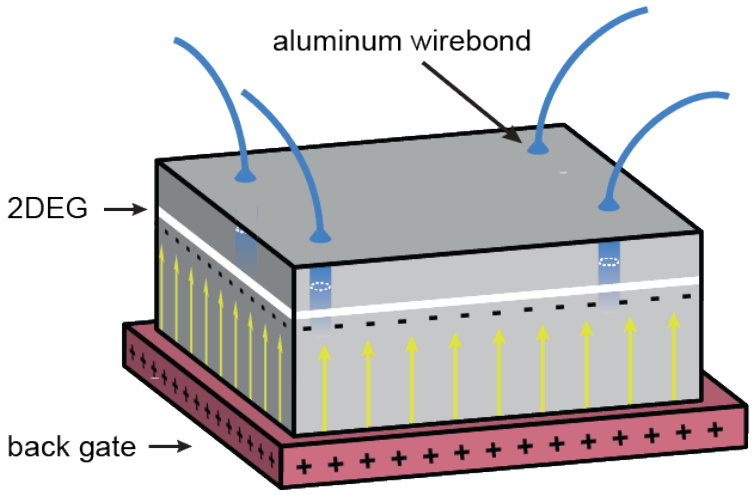

Figure 4.2. Back-gated perovskite oxide heterointerface. A positively charged conductive backgate polarizes the strontium titanate substrate, inducing a change in the charge carrier density at the interface.

When a positively charged back gate voltage is applied to the strontium titanate side of γ-Al_2O_3/$SrTiO_3$, the crystal becomes polarized due to its high dielectric constant (Figure 4.2). If one measures the capacitance between the conductive interface and the back gate using methods described in Chapter 2, the dielectric constant can be calculated. From the experimental value of the dielectric constant and knowledge of the sample area, the expected change in carrier density can be calculated using a parallel plate capacitor model.

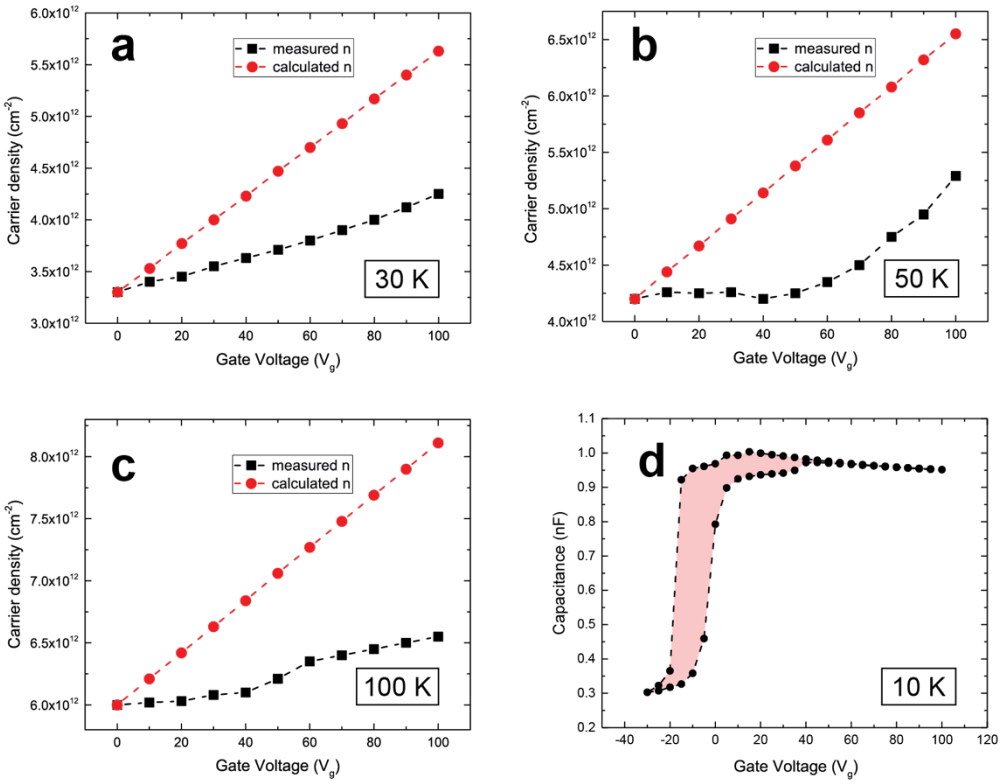

Figure 4.3. Gate voltage dependence on carrier density at a γ-Al_2O_3/$SrTiO_3$ interface. Measurements (shown in black) were collected with Hall measurements while increasing V_g. Calculations were completed using predictions to the carrier density given by the parallel plate capacitor model, added to $n(V_g = 0\ \text{V})$. A difference between measured values and calculated values is shown at 30 K (a), 50 K (b), and 100 K (c). (d) Gate voltage dependence of capacitance of the $SrTiO_3$ on a γ-Al_2O_3/$SrTiO_3$ sample at 10 K. Hysteretic behavior is expected due to the polarizability of strontium titanate. Capacitance was measured using a 50-200 Hz AC signal.

In order to calculate the expected change in carrier density for a γ-Al_2O_3/$SrTiO_3$ heterointerface, the dielectric constant needs to be measured. This can be achieved by directly measuring the capacitance between the back gate and the interfacial conductive layer. Figure 4.3d shows the typical behavior of $SrTiO_3$ capacitance vs back gate at low temperatures. A hysteretic behavior is observed due to the polarizibility of $SrTiO_3$. Although it is expected that the capacitance increases with gate voltage, a crossover occurs near 40 V, above which the system switches from one- to two-carrier transport.[74] This effect is well documented and is also observed in longitudinal magnetoresistance data of $LaAlO_3$/$SrTiO_3$.

From capacitance measurements, the dielectric constant can be calculated, essentially providing an experimental value for ε_r. Using the parallel plate capacitor model, the capacitance, C, can be found using

$$C = \frac{\varepsilon_r \varepsilon_0 A}{d}, \qquad \text{Equation 4.1}$$

where ε_0 is the vacuum permittivity, A is the area of the capacitor plates, and d is the distance between the plates. In the samples measured in this experiment, $A = 5{\times}5$ cm^2 and $d = 5$ mm. Using the data from Figure 4.3d, the dielectric constant of $SrTiO_3$ with no electric field applied at 10 K is 1810 to 2260, depending on the sweep direction of the backgate. This agrees well with previously measured values of the dielectric constant of strontium titanate.

4.3 Immobile charge carriers

The expected change in carrier density can also be obtained from measured capacitance values. Using the definition of capacitance, $Q = CV$ and noting that the

capacitance is a function of gate voltage, one can calculate the expected interfacial charge on a gated $SrTiO_3$ device and derive the formula for the carrier density as a function of gate voltage V_g,

$$\Delta n = \frac{Q(V_g)}{eA} = V_g \frac{C(V_g)}{eA}, \qquad \text{Equation 4.2}$$

where e is the fundamental charge of an electron. The total calculated carrier density predicted through capacitance measurements is then simply

$$n = \Delta n + n(V_g = 0). \qquad \text{Equation 4.3}$$

Additionally, the carrier density can simply be measured using the Hall effect, as explained in Chapter 2. Figure 4.3a-c shows the carrier density measured using the Hall effect compared to the carrier density calculated using Equations 4.2 and 4.3. Clearly there is a discrepancy between the model and the experiment.

Currently, this inconsistency can only be speculated upon. It is evident that the parallel plate capacitor model fails to accurately represent the backgating behavior of γ-$Al_2O_3/SrTiO_3$, but where it fails is a problem yet to be solved. The most reasonable explanation for the discrepancy is that involving immobile charge carriers. There may be an increase in charge at the interface of the strontium titanate, though that does not necessarily translate to an increase in *mobile* charge carriers at the interface. If, for instance, a depletion region is formed in the strontium titanate substrate as a result of the electric field, it is feasible that immobile charge carriers be present, increasing the magnitude of the capacitance measured. As it stands, more charge carriers are expected at the heterointerface due to backgating.

4.4 Mott insulating behavior

Although band theory has been widely successful, its failure to predict Mott insulators reminds us that no theory should never be treated as complete. For example, many transition metal monoxides, such as NiO, MnO, and CoO, were predicted to be band insulators through band theory. However, experimental measurements of these materials showed insulating behavior and easily disrupted the completeness of band theory. The electron-electron interaction is not considered when calculating the band structure, which only describes single electron states. Insulating behavior is expected in most transition metal monoxides when considering electron-electron interactions in the theoretical framework. These materials are known as Mott insulators.

Band theory (using the tight-binding approximation) predicts that the band width of a material increases as the atomic spacing is reduced. This occurs since more atomic orbitals overlap with closer lattice spacing. In this same model, electrical conduction is described as valence electrons hopping from one atom to another, essentially ionizing neighboring atoms ($X + X \rightarrow X^+ + X^-$). The energy cost for one electron hopping to another atom (conduction) is high and is known as the Hubbard energy, denoted as U. The Hubbard energy follows

$$U = I - A, \qquad \text{Equation 4.4}$$

where I is the energy required to ionize an atom (energy to create X^+) and A is the energy released by the donor atom (energy to create X^-) or the electron affinity. Consider a half-filled band, one therefore predicted to be metallic. When the energy for electron hopping is less than that of the band width, the state is metallic and electron hopping is allowed.

However, when the hopping energy is lower than the band width, electron hopping is forbidden and conduction never occurs. In other words, a Mott insulator is that where conduction takes place via atomic ionization, and the energy to ionize an atom in the material, U, is greater than width of the conduction band. In a Mott insulating state, electrons tend to minimize the Coulomb repulsion between each other by staying put on a lattice site. As lattice sites are filled up, the Coulomb repulsion (essentially I) increases, and the state becomes more insulating.

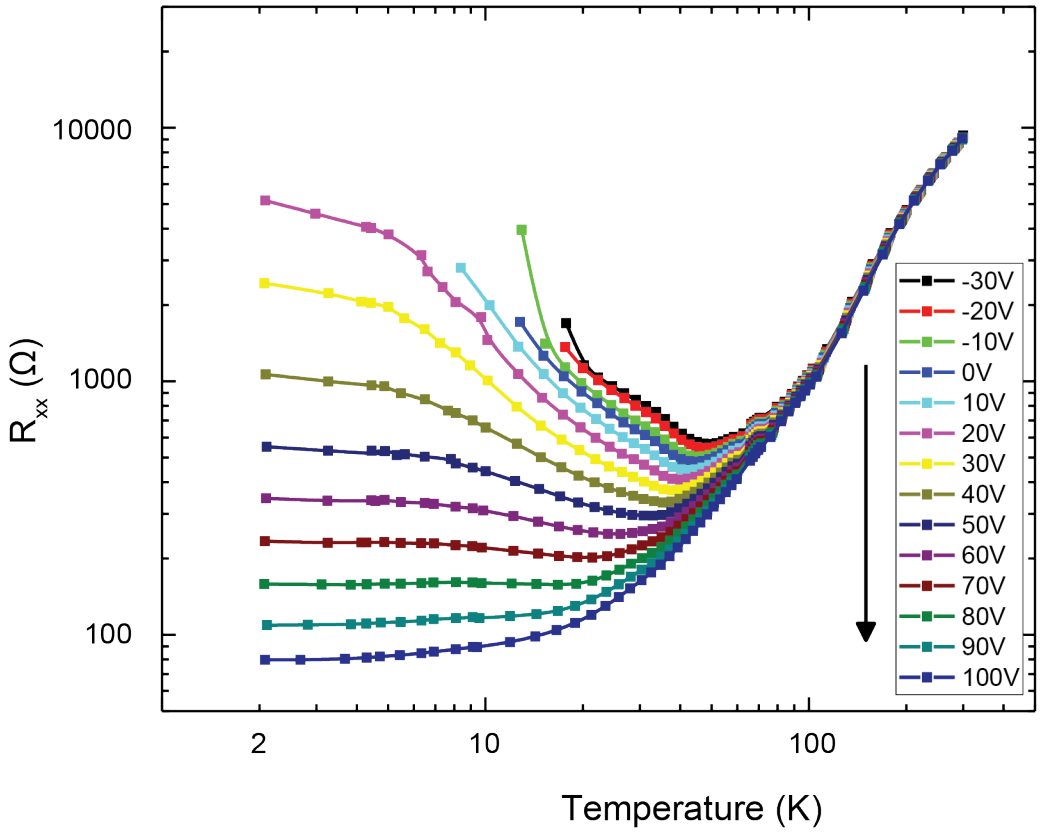

Figure 4.4. Temperature dependent resistance of a γ-Al_2O_3/$SrTiO_3$ interface. The sample is backgated with an increasing voltage from -30 V to 100 V.

Mott insulators can be thought of as electronic correlation-induced insulators. Even at zero temperature, these materials will exhibit non-zero resistivity despite the lack of

phonon scattering and the nature of the band structure. Therefore, the temperature dependent resistance, *R(T)*, shows a saturation at lower temperatures, neither increasing nor decreasing below a certain temperature. This effect can be seen in Figure 4.4 and is typically a "smoking gun" for Mott insulators.

The results of Figure 4.4 were collected for an increasing backgate voltage while cooling down the sample. Due to the hysteresis in the dielectric constant and therefore added carrier density of strontium titanate, resistance curves collected with a decreasing backgate voltage differ slightly from Figure 4.4. In addition, temperature dependent hysteresis at ~100 K appeared in every resistance curve collected while warming the sample up. Measurements collected with decreasing temperature are shown in Figure 4.4.

To date, this is the first measurement of a metal-to-insulator transition in a γ-$Al_2O_3/SrTiO_3$ heterointerface, and the resemblance to a metal-to-Mott insulator transition is uncanny. However, temperature dependence of resistance is not a definitive signature of metal-to-insulator versus metal-to-Mott insulator. The mechanism of this transition needs much more research focus, as these results are preliminary and the discussion is speculative. The measured behavior is intriguing, as neither Al_2O_3 nor $SrTiO_3$ is a not Mott insulator. Still, the result provides the first insight into the metallic and insulating states of γ-$Al_2O_3/SrTiO_3$ heterointerfaces at low temperatures and the immobile charge carriers induced through backgating strontium titanate.

Chapter 5: Anisotropic electronic transport in an oxide heterointerface

The crystal structure of $SrTiO_3$ transitions from cubic to tetragonal at 105 K.[75,76] In the tetragonal phase, striped domain walls form, which separate regions of different crystallographic domains. This structural phase transition plays an important role in the two-dimensional conduction found at oxide heterointerfaces, including the interface of $LaAlO_3$ and TiO_2-terminated $SrTiO_3$ (LAO/STO). Understanding the effects of the anisotropy of the tetragonal phase and related domain boundaries on the electronic properties of the interface is a vital step in engineering LAO/STO heterointerfaces with higher electron mobilities at low temperatures. Recent indirect measurements of striped tetragonal domains have shown enhanced conductivity parallel to the domain walls.[77] However, the fundamental physics of conduction both along and across domain walls is still poorly understood. The following experimental and simulated results show anisotropic electronic transport in LAO/STO samples split by single domain walls. By reducing the spatial size of the conductive interface to less than 400 μm^2, the anisotropy of interfacial electron conduction in relationship to the domain wall direction was characterized. The four-wire conductivity was enhanced when measured perpendicular to a domain wall, which arises under the structural phase transition temperature upon cooling below 100 K. Simulations of a conductive area that is split by regions of lower stripes of resistivity show good quantitative agreement with the experimental results.

5.1 Cubic-to-tetragonal phase transition in $LaAlO_3/SrTiO_3$

Lanthanum aluminate/strontium titanate heterointerfaces show great promise in the field of semiconductor technology. Since the discovery of quasi-two-dimensional conduction between $LaAlO_3$ and $SrTiO_3$ in 2004, LAO/STO heterointerfaces have quickly become one of the fastest growing, most competitive research fields in condensed matter physics.[9] Researchers soon began uncovering many exotic phenomena that can be observed in LAO/STO such as giant persistent photoconductivity,[57] the existence of ferromagnetism with superconductivity,[78] and large in-plane magnetoresistance.[56] Thanks to the promise and success of LAO/STO, perovskite oxide heterostructures are experiencing a significant boom in research focus. $Al_2O_3/SrTiO_3$,[66] bare $SrTiO_3$,[79] $(Nb,Sr)/SrTiO_3$,[80] and $MgO/SrTiO_3$[81] are just a few of the many promising materials that have been realized due to this concentration on oxide electronics.

Along with numerous physical phenomena, perovskite oxide heterointerface systems boast complexities that rival high-T_c superconducting systems. Oxygen growth pressure,[15,77,82,83] La/Al stoichiometry,[84] cation intermixing,[85,86] and substrate growth temperature[87] are simply a few of the many variables that affect interfacial conduction in LAO/STO. In addition, crystal domain boundaries in the STO layer of LAO/STO have been found to create regions of striped potential modulations.[72,77] Other inhomogeneities such as magnetic and superconducting have been observed in LAO/STO.[78,88] In this chapter, it is shown that crystal domain walls significantly affect the transport properties of lanthanum aluminate/strontium titanate heterointerfaces and should thus be considered in future electrical transport experiments.

Structural phase transitions in $SrTiO_3$ have been widely understood since the 1960s.[75] Above a critical temperature ($T_c \sim 105$ K), strontium titanate has a cubic crystal structure. Below T_c, it undergoes a structural phase transition to a non-polar tetragonal crystal phase, extending one of its crystal axes. It should be noted that $SrTiO_3$ is known to undergo a structural phase transition near 55 K, transitioning to an orthorhombic phase. However, the electronic behavior of strontium titanate shows no change near that temperature, so it is considered irrelevant to the current discussion. Though this transition is well documented,[75,89–91] its effect on the transport properties of STO or Nb doped STO is often overlooked. More importantly, the transition's role on the transport properties on the ever-popular LAO/STO heterointerfaces has had very little consideration.

Through optical means and transport measurements, the cubic-to-tetragonal structural phase transition can be observed in LAO/STO. Using polarized microscopy, the tetragonal crystal domains in LAO/STO are easily imaged and characterized.[72,77,92] Striped tetragonal domains are revealed under T_c and are 20 - 40 μm wide, sometimes running the entire length of the sample. In a recent study, stripes of high and low conductivity were found parallel to the striped domains.[77] Large, anomalous piezoelectricity has also been related to the formation of tetragonal domains of strontium titanate.[72] Although these studies are extremely insightful, they do not investigate the direct effect of the tetragonal domains on the electronic transport properties in LAO/STO.

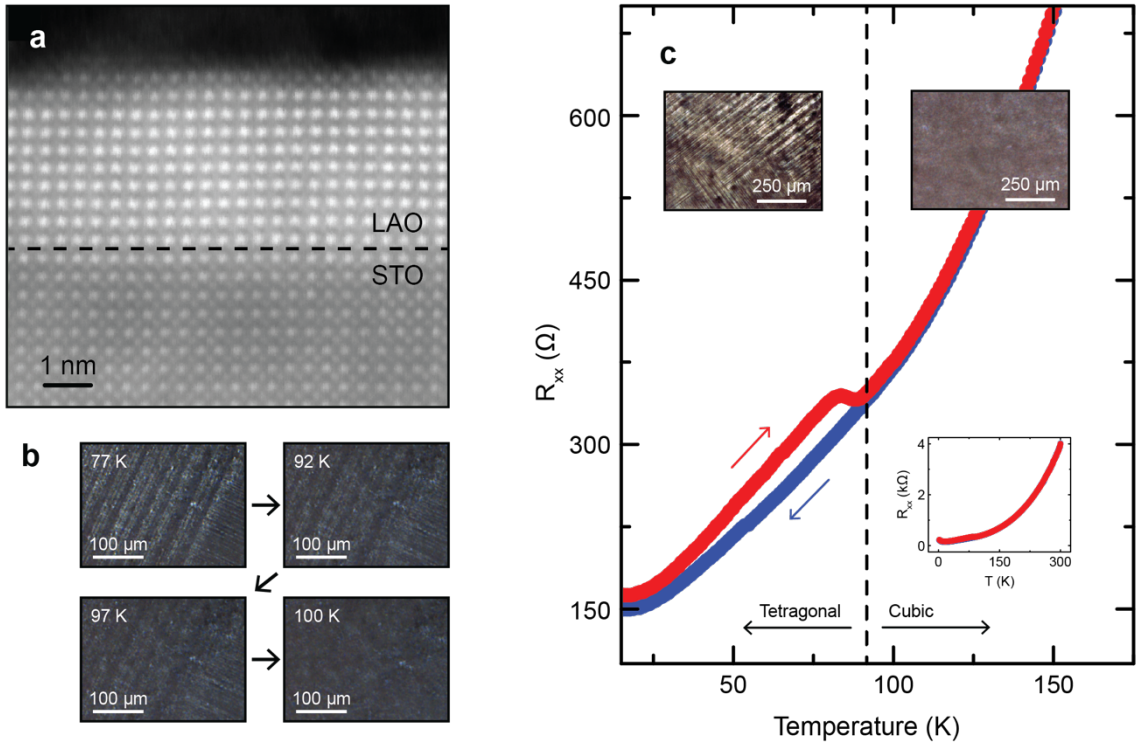

Figure 5.1. Overview of the cubic-to-tetragonal phase transition in LAO/STO. (a) STEM image of LAO/STO interface. Imaged sample has 10 unit cells of LAO and was grown by PLD in 10^{-4} Torr O_2 partial pressure. (b) Polarized transmission microscopy images of LAO/STO showing tetragonal domains at different temperatures. Tetragonal domain walls disappear between 97 K and 100 K. (c) Temperature dependent resistance of an etched 10 u.c. LAO/STO sample. Arrows indicate temperature sweep direction, showing hysteresis below the transition temperature. Insets show temperature dependent resistance from 2 K – 300 K and polarized microscopy images of the sample in the tetragonal and cubic phases.

Characterization of LAO/STO typically is done on 5 mm x 5 mm samples grown in O_2 partial pressures 10^{-4} or 10^{-5} Torr. The LAO/STO interface with minimal La/Sr intermixing can be viewed using STEM imaging (Figure 5.1a). Conducting LAO thicknesses of 8 and 10 unit cells were studied, and a complete table of sample characteristics can be found in Table 5.1.

Sample number	LAO thickness	O_2 partial pressure	Domain wall ∠	$R_{parallel}$ / R_{perp}	Area	Carrier density (10 K)

10.1	10 u.c.	10^{-4} Torr	90°	1,000-70,000	40x40 μm^2	3.64×10^{13} cm^{-2}
10.2	10 u.c.	10^{-4} Torr	90°	16	30x30 μm^2	2.59×10^{13} cm^{-2}
10.3	10 u.c.	10^{-4} Torr	90°	10	20x20 μm^2	3.21×10^{13} cm^{-2}
8.1	8 u.c.	10^{-5} Torr	90°	15	30x30 μm^2	n/a
10.4	10 u.c.	10^{-4} Torr	45°	1.45	20x20 μm^2	3.49×10^{13} cm^{-2}
10.5	10 u.c.	10^{-5} Torr	none	1.25	10x10 μm^2	2.50×10^{15} cm^{-2}
10e.615	10 u.c.	10^{-4} Torr	none	1.35	20x20 μm^2	n/a

Table 5.1. Collection of patterned and measured samples. All seven samples studied were grown using pulsed laser deposition. A LAO thickness of 10 u.c. provided reliable interfacial conduction in all growth conditions, though a sample with 8 u.c. LAO thickness was studied as well, providing comparable results. Samples grown at a lower O_2 partial pressure showed substantially higher carrier densities due to the increase in oxygen vacancies in the STO crystal. Sample 10a.615 was patterned with eight contacts, allowing for multiple measurement configurations across the same domain wall. All resistances reflect measurements taken at 2 K.

A portable cryostat with an optical window allowed for the imaging of domain walls in the patterned samples via transmission polarized light microscopy (Fig. 5.1b) using techniques originally described in previous reports.[85] The domain walls are on average ~30 μm apart, which agrees with previously published results.[77] Contrary to previous reports, no change in the location of domain walls was observed due to thermal cycling between 77 K – 125 K (Figure 5.2). Warming and cooling of the samples does not change the direction or placement of the domain walls. Figure 5.1b shows the disappearance of tetragonal domains between 77 K – 100 K. The formation and disappearance of striped domains were studied at temperature increments of 1 K in equilibrium conditions after waiting more than 60 seconds. The disappearance of domain walls is observed near 97 K – 100 K with no change at 105 K, suggesting a lower cubic-to-tetragonal temperature than previous reports of $SrTiO_3$[76] and LAO/STO.[72,77]

Figure 5.2. Striped tetragonal domain imaging through thermal cycling. Multiple LAO/STO samples were imaged through the structural phase transition prior to patterning and etching. Samples were carefully heated from 77 K to 125 K and subsequently cooled back down to 77 K. No change in the domain wall configuration was observed due to thermal cycling through the cubic-to-tetragonal phase transition.

5.2 Phase transitions affecting electronic transport

Supporting the disappearance of tetragonal domains between 97 K – 100 K is a hysteresis effect observed in the temperature dependent resistance measurements. Cool-down and warm-up resistance curves diverged below 95 K (Fig. 1c), where $R_{warm\text{-}up} \neq R_{cool\text{-}down}$. In some instances, the warm-up resistance curve changed direction around 95 K, decreasing with increasing temperature. Resistance and polarized imaging measurements were conducted simultaneously, and the disappearance of domain walls was directly correlated to the disappearance of hysteretic resistance, also consequently supporting the prior conclusion regarding the lower phase transformation temperature than the previously reported values. This effect was observed in all patterned and unpatterned LAO/STO samples. A further study of domain wall behavior through thermal cycling would provide valuable information on the nature of the cubic-to-tetragonal phase transition, though such work is beyond the scope of these studies.

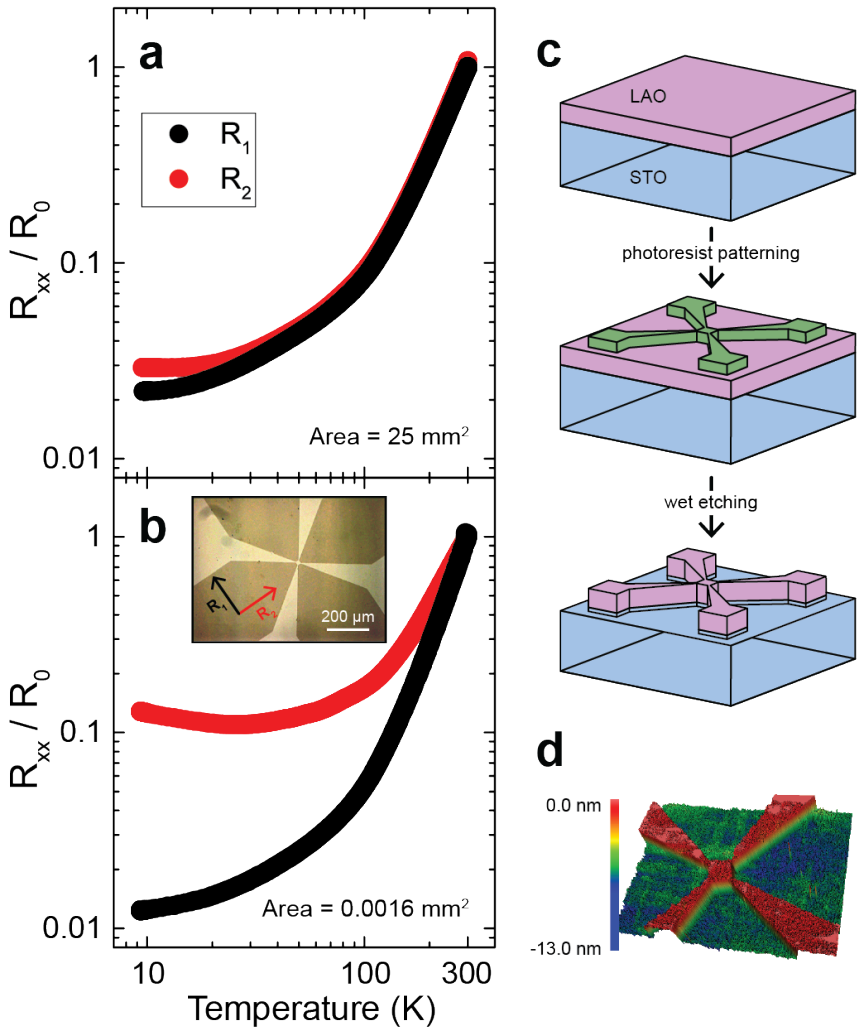

Figure 5.3. Normalized temperature dependent resistance for a 10 u.c. LAO/STO sample before (a) and after (b) etching. R_1 and R_2 indicate perpendicular current orientations (see inset). Inset is a standard microscopy image of the etched Van der Pauw pattern. The process of etching the sample is shown in (c). A photoresist mask is patterned on bare LAO/STO, which is subsequently etched. The mask is removed, leaving only the conductive interface covered by the pattern. After the process is complete, the sample topography was imaged using an optical profilometer (d).

Under the cubic-to-tetragonal transition temperature, twin domains averaging 30 μm wide run parallel to each other and are split by domain walls.[77] The direction of striped twin boundaries changes at antiphase boundaries throughout the sample, and any anisotropy in carrier transport due to domains and domain boundaries is averaged out over

measurement areas much larger than the domain wall spacing. To study the anisotropy of electrical transport due to domain orientation, the measurement area was reduced to the order of the domain size. Photolithography and wet etching techniques were performed on pulsed laser deposition grown LAO/STO samples grown by pulsed laser deposition to reduce the spatial size of the conductive interface to 20 x 20 μm^2 - 40 x 40 μm^2 Van der Pauw squares (Fig 5.3c). Normalized temperature dependent resistance is shown in Figure 5.3 before (a) and after (b) reducing the conductive area. R_1 and R_2 are longitudinal resistances with different current flow directions (Fig 5.3b inset). Directionally dependent anisotropy was observed in two-wire and four-wire resistance at low temperatures that was not present before the sample size was reduced. The anisotropy significantly grows with decreasing temperature below the cubic-to-tetragonal transition temperature.

5.3 Anisotropic resistance due to tetragonal domain walls

Reflective light microscopy was used to image the conducting Van der Pauw patterns post-etching. Images of domain walls were overlaid with the etched patterns to obtain a clear picture how domain walls intersected the Van der Pauw squares (Fig 5.4a-c). Transport measurements reveal homogenous resistance from room temperature down to below 105 K for all samples. Striped domain walls appear below the transition temperature, which split most samples by 0° or 45°, as illustrated in Figure 5.4.

In addition to temperature dependent hysteresis in resistance measurements, the resistance itself showed dependence on domain walls in the tetragonal phase, and their orientation with respect to the measurement direction. When the crystal structure of STO is cubic (300 K - 105 K), isotropic resistance is measured

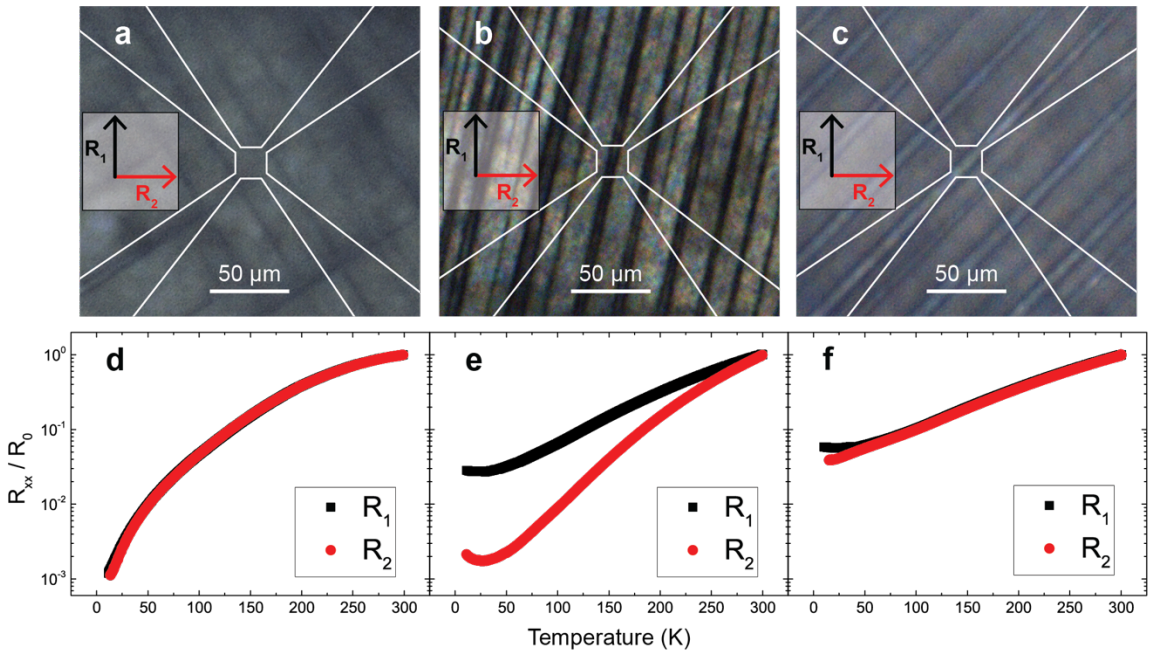

Figure 5.4. Tetragonal domain overlays and corresponding temperature dependent resistance. (a, b, c) Conductive Van der Pauw patterns created using photolithography and wet etching are outlined in white. Images and data show samples at 77 K with no domain walls, a domain wall at 90°, and a domain wall at 45°, respectively. Images (d, e, f) show the normalized temperature dependent longitudinal resistance for two measurement orientations. Resistance is isotropic with no domain wall (a) and a 45° wall (c) and is anisotropic with a 90° domain wall (b). All samples are 10 u.c. thick and grown at 10^{-4} Torr O_2 pressure.

in all samples (patterned and unpatterned), finding R_1 roughly equivalent to R_2 Where R1 and R2 measurement directions are orthogonal to each other. Measurement symmetry was lost when the striped domains and thus the domain walls are 90° or 0° (anisotropic) to the two orthogonal measurement directions (R1 and R2) but was preserved when they were at a 45° angle (isotropic). Figure 5.4 shows images of tetragonal domain walls overlaid with the conductive Van der Pauw patterns and their comparative resistance measurements. In some patterned samples no observable domain walls were observed either due to the size or placement of the Van der Pauw pattern. Such samples remained isotropic down to 2 K,

arguably due to the lack of a domain wall (compare Fig. 5.4a, d). In all patterned samples with striped domains 90° to the measurement direction, there is over a 10 times difference between R_1 and R_2 at low temperatures (Fig. 5.4b, e), where the greater resistance (R1) is parallel to the striped domain direction. When LAO/STO crystals were patterned 45° to the [001] direction, samples were created with striped domains 45° to the measurement direction (Fig. 5.4c). Samples with this orientation showed no anisotropy below 105 K (Fig. 5.4f), similar to the lack of anisotropy in samples with no domain walls.

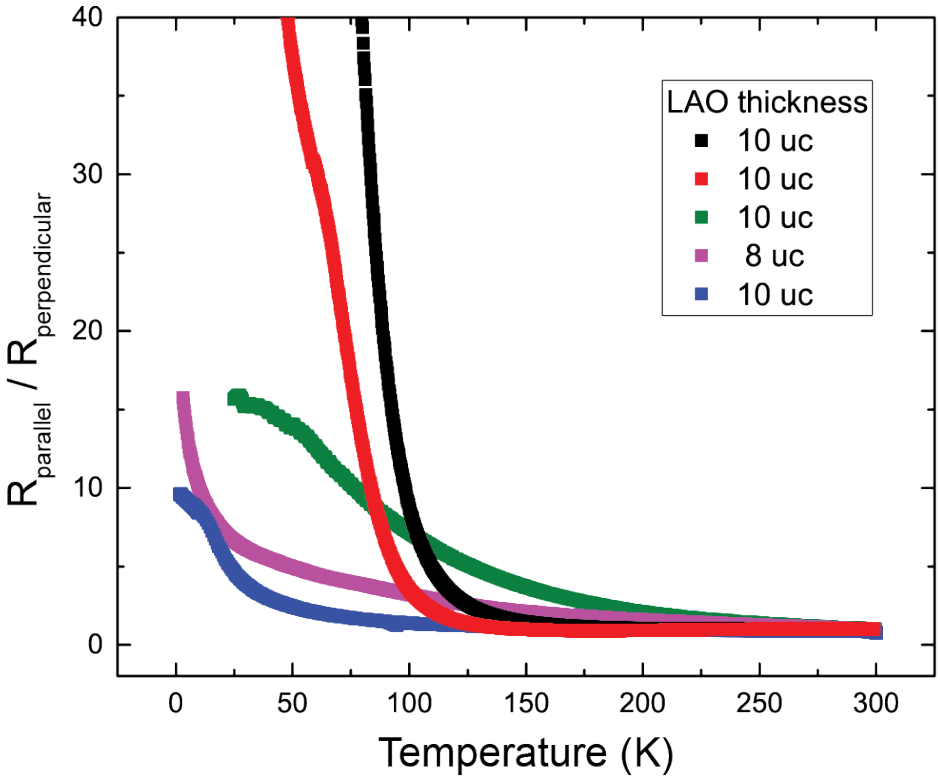

Figure 5.5. Anisotropy strength in various LAO/STO samples split by a domain wall at 90°. All samples are 8-10 u.c. LAO thick and grown at 10^{-5} or 10^{-6} Torr O_2 pressure. Samples with a 90° domain wall show an anisotropy of 1-6 orders of magnitude between $R_{parallel}$ and $R_{perpendicular}$. Y-axis scale has been reduced for clarity.

The strength of anisotropic resistance is best illustrated by plotting the relative difference between parallel and perpendicular resistances. All data collected on patterned samples where the striped domains were 90° to the measurement direction is presented in Figure 5.5. At 10 K, the anisotropy strength was less than 1.5 for samples with no domain wall or with domain walls at a 45° angle to the measurement direction. $R_{parallel}$ is defined as the four-wire resistance measured parallel to a domain wall and $R_{perpendicular}$ is defined as the four-wire resistance measured perpendicular or through a domain wall. In all samples where the domain wall is 90° to the measurement direction, isotropic behavior is observed at room temperature. Anisotropy grows as the temperature is lowered, and the strength is larger than an order of magnitude in all samples at base temperature, which is attributed to the creation of tetragonal domain walls. In two of the four samples exhibiting anisotropy, $R_{parallel}$ / $R_{perpendicular}$ is greater than 1000. The scale for Figure 5.5 is truncated to better illustrate all of the collected data curves.

5.4 Electrostatic simulation of domain walls

Using electromagnetic simulation software QuickField, distribution of current flow and electrostatic potential in a Van der Pauw square is calculated (Figure 5.6). In an effort to qualitatively illustrate the observed behavior, the domain wall is modeled as a wide region with lower resistivity and a wide region with higher resistivity. Domains themselves are assumed to be isotropic in this simulation, and calculations with anisotropic domains may increase the strength of the anisotropic behavior.

Calculations showed that when the electric field in an area split by a region of higher resistivity, $R_{parallel} > R_{perpendicular}$, which disagreed with the observed behavior. In such a model, parallel current flow was greatly reduced between voltage contacts, thereby

reducing $R_{parallel}$. Similarly, $R_{perpendicular}$ was enhanced due to an enhancement of electrical current between voltage contacts. However, conductive area split by a region of lower resistivity gives qualitative agreement with our experiments. Parallel current flow was

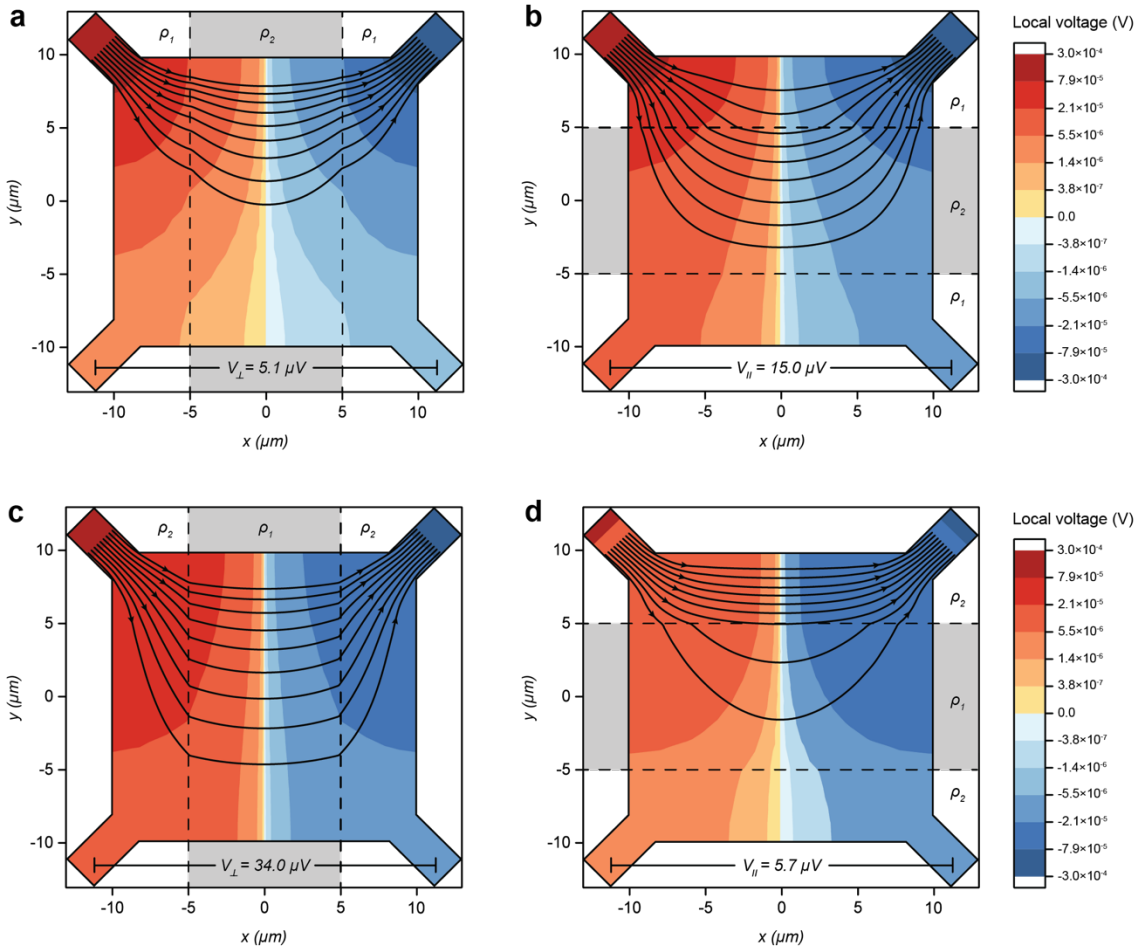

Figure 5.6. Simulated current flow and voltage distribution for inhomogeneous 20 μm × 20 μm Van der Pauw patterns. The conductive squares are split by 10 μm wide regions with different resistivity, where ρ_1 = 25,000 Ω and ρ_2 = 10,000 Ω. Total current flow is 10 nA in all simulations and is represented with streamlines. Simulated samples in (a) and (b) are split by more conductive regions oriented perpendicular and parallel to the current flow, respectively. When a conductive region splits the sample, measured $V_{parallel}$, and therefore $R_{parallel}$ is greater than $V_{perpendicular}$ and $R_{perpendicular}$, and the sample shows enhanced conductance perpendicular to the conductive region. However, when the samples are split by a more resistive area as in (c) and (d), the sample shows enhanced conduction parallel to the more resistive region.

enhanced between voltage contacts. In this picture, $R_{parallel} < R_{perpendicular}$. Note, this was only observed when the resistivity difference between two regions were less than approximately ten times. As the difference increases, a crossover occurred where the behavior switches and $R_{parallel} > R_{perpendicular}$. Nevertheless, the anisotropy strength is calculated to be $R_{parallel} / R_{perpendicular} \approx 3$.

The physical source of reduced resistivity caused by domain walls is still a question to be answered, and as the observed anisotropic strength is 10 to 7×10^4, additional physical effects must be present. Crystal discontinuities at twin boundaries may cause an increase in oxygen vacancies, leading to an increase in free charge carriers near domain walls, although twin boundaries in low-energy STO domain walls are not expected to be charged.[25]

The structure of domain walls in STO may also be affected by the presence of LAO. The lattice constant of STO is slightly larger than LAO, so interfacial strain can enhance strain and flexoelectric coupling in the domain walls. The strain gradient in STO domain walls results in flexoelectric coupling, which gives rise to polarization across the walls.[93,94] One may expect an accumulation of charge near domain walls due to domain wall polarization. A picometer resolved TEM study has confirmed the buckling of oxygen and lanthanum atoms in LAO,[95] and the lengthening of TiO_6 octahedra in STO have been observed.[96] These small effects may effect the formation of tetragonal domain walls in STO. A detailed theoretical study on the physical and electronic properties of twin boundaries in LAO/STO would provide valuable insight into these experimental results.

Chapter 6: Summaries and perspectives

Two-dimensional electronic systems are invaluable tools to test the limits of physics. Reducing dimensionality does not reduce the complexity of the physics, it enriches it. Two-dimensional physics can be fundamentally different between classical, three-dimensional physics. Take, for example, the quantum Hall effect, the spin Hall effect, particle braiding, and the strong electron-electron correlation discovered in two-dimensional systems. Continuing to study these systems in both new and established materials will uncover more novel phenomena not predicted by theory. As two-dimensional electronics continues to be a mainstream research field, the collective understanding and intuition for electronic transport in all dimensionality will continue to grow.

Not only do two-dimensional systems increase the knowledge and understanding of electronic transport at a fundamental level, they provide new avenue for technological advancement. The level of bandgap engineering that is required for realizing a two-dimensional system in two-dimensional semiconductors has already provided valuable knowledge toward bandgap engineering in all systems. Trial and error, DMFT calculations, and high-precision/high-purity growth methods all contribute towards the collective knowledge used in engineering more advanced semiconductor devices. In addition, two-dimensional systems could see a future place in technological applications. Conventional semiconductors exhibit a usually unavoidable trait: as the carrier concentration increases, the charge mobility suffers. With use of modulation doping for example, two-dimensional electron gasses exhibit very high charge carrier concentrations without much reduction in the carrier mobility. This is exciting for application-based devices since higher mobilities translates to better, faster electronics.

The impact of short-range disorder scattering on the nonmonotonic temperature dependent resistance has revealed new insights on the relationship between short-range disorder potential and two-dimensional metallic conduction. By changing the aluminum fraction in $Al_xGa_{1-x}As$ barriers, the short-range disorder potential was systematically changed. The strength of the anomalous two-dimensional metallic conduction is suppressed as the aluminum fraction is increased. In addition, a universality in the metallic temperature dependent resistance is shown, even with the inclusion of a non-monotonic resistance peak. Analysis also reveals that an increased aluminum fraction leads to a suppressed characteristic temperature T_0, below which the metallic conduction occurs.

Two-dimensional electronic transport in perovskite oxide heterointerfaces has also been considered. Similar to the gate effect induced change in carrier density in Chapter 3, Chapter 4 showed that γ-$Al_2O_3/SrTiO_3$ heterointerfaces exhibit similar behavior. This, however, is a more complex effect than in GaAs quantum wells since the large dielectric constant of strontium titanate is used. Due to the polarized nature of strontium titanate, the field effect strongly depends upon the direction of sweeping the back gate voltage. Most likely due to a depletion region in the substrate, less mobile charge carriers are induced in the quasi-two-dimensional electron gas than expected from a parallel plate capacitor model. Regardless, a strong field effect is observed, which can tune the electronic behavior from a metallic to insulating state. The temperature dependent resistance is observed to have characteristics of a Mott insulator, but more study is required to conclude a true Mott insulating state.

Finally, electrical transport through single domain walls in LAO/STO has been studied by reducing the conductive interface to micron scales. Domain wall location was verified

using polarized light microscopy. Anisotropic resistance is observed only below the cubic-to-tetragonal phase transition temperature and only in samples where striped domains were 90° to the measurement direction. Samples with no domain walls or where the domain walls were 45° to the measurement direction remain isotropic down to temperatures as low as 2 K. Four-wire resistance is significantly lower when measuring perpendicular rather than parallel to the domain wall, and the anisotropy strength was observed to be between 10 and 7×10^4. This behavior has been qualitatively modeled by treating the sample as being split by conductive stripes, though more theoretical work must be completed in order to better understand these results.

Bibliography

1. Abrahams E. Scaling theory of localization: Absence of quantum diffusion in two dimensions. Phys Rev Lett. 1979;

2. Kravchenko S, Kravchenko G. Possible metal-insulator transition at B= 0 in two dimensions. Phys Rev B. 1994;

3. Noh H, Lilly M, Tsui D, Simmons J. Linear temperature dependence of conductivity in the apparent insulating regime of dilute two-dimensional holes in GaAs. Phys Rev B. 2003;

4. Lilly M, Reno J, Simmons J. Resistivity of dilute 2D electrons in an undoped GaAs heterostructure. Phys Rev Lett. 2003;

5. Ando T, Matsumoto Y, Uemura Y. Theory of Hall effect in a two-dimensional electron system. J Phys Soc Japan. 1975;

6. Klitzing K, Dorda G, Pepper M. New method for high-accuracy determination of the fine-structure constant based on quantized Hall resistance. Phys Rev Lett. 1980;

7. Tsui D, Stormer H, Gossard A. Two-dimensional magnetotransport in the extreme quantum limit. Phys Rev Lett. 1982;

8. Laughlin R. Anomalous quantum Hall effect: an incompressible quantum fluid with

fractionally charged excitations. Phys Rev Lett. 1983;

9. Ohtomo A, Hwang HY. A high-mobility electron gas at the LaAlO3/SrTiO3 heterointerface. Nature. 2004;427(6973):423–6.

10. Ando T. Self-Consistent Results for a GaAs/Al x Ga1-x As Heterojunciton. II. Low Temperature Mobility. J Phys Soc Japan. 1982;

11. Watson J, Mondal S, Gardner G. Exploration of the limits to mobility in two-dimensional hole systems in GaAs/AlGaAs quantum wells. Phys Rev B. 2012;

12. Pavlenko N, Kopp T, Tsymbal E. Oxygen vacancies at titanate interfaces: Two-dimensional magnetism and orbital reconstruction. Phys Rev B. 2012;

13. Huijben M, Brinkman A, Koster G. Structure–property relation of SrTiO3/LaAlO3 interfaces. Adv Mater. 2009;

14. Basletic M, Maurice J, Carrétéro C. Mapping the spatial distribution of charge carriers in LaAlO3/SrTiO3 heterostructures. Nat Mater. 2008;

15. Kalabukhov A, Gunnarsson R, Borjesson J, Olsson E, Claeson T, Winkler D. Effect of oxygen vacancies in the SrTiO3 substrate on the electrical properties of the LaAlO3/SrTiO3 interface. Phys Rev B. 2007;75(12).

16. Salluzzo M, Cezar J, Brookes N. Orbital reconstruction and the two-dimensional

electron gas at the LaAlO 3/SrTiO 3 interface. Phys Rev Lett. 2009;

17. Gränz B, Korshunov S, Geshkenbein V, Blatter G. Competing structures in two-dimensional trapped dipolar gases. Phys Rev B. 2014;

18. Morozovska A, Eliseev E, Glinchuk M. Impact of free charges on polarization and pyroelectricity in antiferrodistortive structures and surfaces induced by a flexoelectric effect. Ferroelectrics. 2012;

19. Abrahams E, Kravchenko S, Sarachik M. Metallic behavior and related phenomena in two dimensions. Rev Mod Phys. 2001;

20. Lee P, Ramakrishnan T. Disordered electronic systems. Rev Mod Phys. 1985;

21. Spivak B, Kravchenko S, Kivelson S, Gao X. Colloquium: Transport in strongly correlated two dimensional electron fluids. Rev Mod Phys. 2010;

22. Kravchenko S, Sarachik M. Metal–insulator transition in two-dimensional electron systems. Reports Prog Phys. 2004;

23. Spivak B, Kivelson S a. Phases intermediate between a two-dimensional electron liquid and Wigner crystal. Phys Rev B - Condens Matter Mater Phys. 2004;70(15):1–8.

24. Spivak B, Kivelson SA. Transport in two dimensional electronic micro-emulsions.

Ann Phys (N Y). 2006;321(9):2071–115.

25. Tanatar B, Ceperley DM. Ground state of the two-dimensional electron gas. Phys Rev B. 1989;39(8):5005–16.

26. Attaccalite C, Moroni S, Gori-Giorgi P, Bachelet GB. Correlation Energy and Spin Polarization in the 2D Electron Gas. Phys Rev Lett. 2002;88(25):256601.

27. Falakshahi H, Waintal X. Hybrid phase at the quantum melting of the Wigner crystal. Phys Rev Lett. 2005;

28. Drummond N, Needs R. Phase diagram of the low-density two-dimensional homogeneous electron gas. Phys Rev Lett. 2009;

29. Clark B, Casula M, Ceperley D. Hexatic and Mesoscopic Phases in a 2D Quantum Coulomb System. Phys Rev Lett. 2009;

30. Qiu R, Gao X, Pfeiffer L, West K. Connecting the Reentrant Insulating Phase and the Zero-Field Metal-Insulator Transition in a 2D Hole System. Phys Rev Lett. 2012;

31. Kuntsevich A, Pudalov V. Comment on “Connecting the Reentrant Insulating Phase and the Zero-Field Metal-Insulator Transition in a 2D Hole System.” Phys Rev Lett. 2013;

32. Qiu R, Gao X. Qiu and Gao Reply. Phys Rev Lett. 2013;

33. Mokashi A, Li S, Wen B, Kravchenko S. Critical behavior of a strongly interacting 2D electron system. Phys Rev Lett. 2012;

34. Kirkpatrick T, Belitz D. Quantum Phase Transition in a Clean Two-Dimensional Electron System. Phys Rev Lett. 2013;

35. Sarma S, Hwang E. The so-called two dimensional metal–insulator transition. Solid State Commun. 2005;

36. Jr AM, Ramirez A, Pfeiffer L, West K. Nonmonotonic temperature-dependent resistance in low density 2D hole gases. Phys Rev Lett. 1999;

37. Gao X, Jr AM, Ramirez A. Weak-localization-like temperature-dependent conductivity of a dilute two-dimensional hole gas in a parallel magnetic field. Phys Rev Lett. 2002;

38. Manfra M, Hwang E, Das Sarma S, Pfeiffer L, West K, Sergent A. Transport and Percolation in a Low-Density High-Mobility Two-Dimensional Hole System. Phys Rev Lett. 2007;99(23):236402.

39. Hanein Y, Meirav U, Shahar D, Li C. The metalliclike conductivity of a two-dimensional hole system. Phys Rev Lett. 1998;

40. Kravchenko S, Simonian D, Mertes K. Classical versus quantum effects in the B= 0 conducting phase in two dimensions. Phys Rev B. 1999;

41. Lai K, Pan W, Tsui D, Lyon S. Linear temperature dependence of the conductivity in Si two-dimensional electrons near the apparent metal-to-insulator transition. Phys Rev B. 2007;

42. Hanein Y, Shahar D, Yoon J, Li C. Observation of the metal-insulator transition in two-dimensional n-type GaAs. Phys Rev B. 1998;

43. Punnoose A, Finkel'stein A. Metal-insulator transition in disordered two-dimensional electron systems. Science (80-). 2005;

44. Camjayi A, Haule K, Dobrosavljević V, Kotliar G. Coulomb correlations and the Wigner–Mott transition. Nat Phys. 2008;

45. Sarma S, Hwang E, Kaminski A. Temperature-dependent magnetization in diluted magnetic semiconductors. Phys Rev B. 2003;

46. Clarke W, Yasin C, Hamilton A. Impact of long-and short-range disorder on the metallic behaviour of two-dimensional systems. Nat Phys. 2008;

47. Zala G, Narozhny B, Aleiner I. Interaction corrections at intermediate temperatures: Longitudinal conductivity and kinetic equation. Phys Rev B. 2001;

48. Qiu R, Gao X, Pfeiffer L, West K. Degenerate versus semidegenerate transport in a correlated two-dimensional hole system. Phys Rev B. 2011;

49. Gao X, Boebinger G, Jr AM. Temperature and magnetic-field-enhanced Hall slope of a dilute 2D hole system in the ballistic regime. Phys Rev Lett. 2004;

50. Andreev A, Kivelson S, Spivak B. Hydrodynamic description of transport in strongly correlated electron systems. Phys Rev Lett. 2011;

51. Sarma S, Hwang E, Li Q. Two-dimensional metal-insulator transition as a potential fluctuation driven semiclassical transport phenomenon. Phys Rev B. 2013;

52. Tiemann L, Gamez G, Kumada N, Muraki K. Unraveling the spin polarization of the ν= 5/2 fractional quantum Hall state. Science (80-). 2012;

53. Oveshnikov L, Kulbachinskii V. Anomalous hall effect in a 2D heterostructure including a GaAs/InGaAs/GaAs quantum well with a remote Mn δ-layer. JETP Lett. 2015;

54. An S, Glinskis S, Kang W, Ocola L. Fabrication of Electronic Fabry-Perot Interferometer in the Quantum Hall Regime. arXiv Prepr. 2014;

55. Gariglio S, Reyren N. Superconductivity at the LaAlO3/SrTiO3 interface. J Phys Condens Matter. 2009;

56. Ben Shalom M, Sachs M, Rakhmilevitch D, Palevski A, Dagan Y. Tuning Spin-Orbit Coupling and Superconductivity at the SrTiO3/LaAlO3 Interface: A Magnetotransport Study. Phys Rev Lett. 2010;104(12).

57. Tebano A, Fabbri E, Pergolesi D, Balestrino G, Traversa E. Room-Temperature Giant Persistent Photoconductivity in SrTiO3/LaAlO3 Heterostructures. ACS Nano. 2012;6(2):1278–83.

58. Thiel S, Hammerl G, Schmehl A. Tunable quasi-two-dimensional electron gases in oxide heterostructures. Science (80-). 2006;

59. Lee M, Williams J, Zhang S. Electrolyte gate-controlled Kondo effect in SrTiO 3. Phys Rev Lett. 2011;

60. Cen C, Thiel S, Hammerl G. Nanoscale control of an interfacial metal–insulator transition at room temperature. Nat Mater. 2008;

61. Chen Y, Trier F, Kasama T, Christensen D. Creation of high mobility two-dimensional electron gases via strain induced polarization at an otherwise nonpolar complex oxide interface. Nano Lett. 2015;

62. Kalabukhov A, Gunnarsson R. Electrical transport properties of polar heterointerface between KTaO3 and SrTiO3. arXiv Prepr. 2007;

63. Li D, Wang Y, Dai J. Tunable electronic transport properties of $DyScO_3/SrTiO_3$ polar heterointerface. Appl Phys Lett. 2011;

64. Reinle-Schmitt M, Cancellieri C. Tunable conductivity threshold at polar oxide interfaces. Nat Commun. 2012;

65. Lee S, Liu Y, Heo J, Gordon R. Creation and control of two-dimensional electron gas using Al-based amorphous oxides/SrTiO3 heterostructures grown by atomic layer deposition. Nano Lett. 2012;

66. Chen YZ, Bovet N, Trier F, Christensen D V, Qu FM, Andersen NH, et al. A high-mobility two-dimensional electron gas at the spinel/perovskite interface of gamma-Al2O3/SrTiO3. Nat Commun. 2013;4.

67. Annadi A, Putra A, Liu Z, Wang X. Electronic correlation and strain effects at the interfaces between polar and nonpolar complex oxides. Phys Rev B. 2012;

68. Perna P, Maccariello D. Conducting interfaces between band insulating oxides: The LaGaO3/SrTiO3 heterostructure. Appl Phys Lett. 2010;

69. He C, Sanders T, Gray M, Wong F. Metal-insulator transitions in epitaxial LaVO 3 and LaTiO 3 films. Phys Rev B. 2012;

70. Moetakef P, Cain T, Ouellette D. Electrostatic carrier doping of GdTiO3/SrTiO3

interfaces. Appl Phys Lett. 2011;

71. Neville R, Hoeneisen B, Mead C. Permittivity of strontium titanate. J Appl Phys. 1972;

72. Honig M, Sulpizio JA, Drori J, Joshua A, Zeldov E, Ilani S. Local electrostatic imaging of striped domain order in LaAlO3/SrTiO3. Nat Mater. 2013;12(12):1112–8.

73. Sidoruk J, Leist J, Gibhardt H. Quantitative determination of domain distribution in SrTiO3—competing effects of applied electric field and mechanical stress. J Phys Condens Matter. 2010;

74. Joshua A, Pecker S, Ruhman J. A universal critical density underlying the physics of electrons at the LaAlO3/SrTiO3 interface. Nat Commun. 2012;

75. Cowley RA. Lattice Dynamics + Phase Transitions of Strontium Titanate. Phys Rev. 1964;134(4a):A981 – +.

76. Lytle FW. X-Ray Diffractometry of Low-Temperature Phase Transformations in Strontium Titanate. J Appl Phys. 1964;35(7):2212 – &.

77. Kalisky B, Spanton EM, Noad H, Kirtley JR, Nowack KC, Bell C, et al. Locally enhanced conductivity due to the tetragonal domain structure in LaAlO3/SrTiO3

heterointerfaces. Nat Mater. 2013;12(12):1091–5.

78. Bert JA, Kalisky B, Bell C, Kim M, Hikita Y, Hwang HY, et al. Direct imaging of the coexistence of ferromagnetism and superconductivity at the LaAlO3/SrTiO3 interface. Nat Phys. 2011;7(10):767–71.

79. Meevasana W, King PDC, He RH, Mo SK, Hashimoto M, Tamai A, et al. Creation and control of a two-dimensional electron liquid at the bare SrTiO3 surface. Nat Mater. 2011;10(2):114–8.

80. Ohta H, Kim S, Mune Y, Mizoguchi T, Nomura K, Ohta S, et al. Giant thermoelectric Seebeck coefficient of two-dimensional electron gas in SrTiO3. Nat Mater. 2007;6(2):129–34.

81. Li JJ, Lv SH, Chen CL, Huang SM, Wang ZC. Interfacial defect complex at the MgO/SrTiO3 heterojunction and its electronic impact. Rsc Adv. 2014;4(92):51002–7.

82. Herranz G, Basletic M, Bibes M, Carretero C, Tafra E, Jacquet E, et al. High mobility in LaAlO3/SrTiO3 heterostructures: Origin, dimensionality, and perspectives. Phys Rev Lett. 2007;98(21).

83. Siemons W, Koster G, Yamamoto H, Harrison WA, Lucovsky G, Geballe TH, et al. Origin of charge density at LaAlO3 on SrTiO3 heterointerfaces: Possibility of

intrinsic doping. Phys Rev Lett. 2007;98(19).

84. Warusawithana MP, Richter C, Mundy JA, Roy P, Ludwig J, Paetel S, et al. LaAlO3 stoichiometry is key to electron liquid formation at LaAlO3/SrTiO3 interfaces. Nat Commun. 2013;4.

85. Chambers SA, Engelhard MH, Shutthanandan V, Zhu Z, Droubay TC, Qiao L, et al. Instability, intermixing and electronic structure at the epitaxial LaAlO3/SrTiO3(001) heterojunction. Surf Sci Rep. 2010;65(10-12):317–52.

86. Qiao L, Droubay TC, Shutthanandan V, Zhu Z, Sushko P V, Chambers SA. Thermodynamic instability at the stoichiometric LaAlO3/SrTiO3(001) interface. J Physics-Condensed Matter. 2010;22(31).

87. Caviglia AD, Gariglio S, Cancellieri C, Sacepe B, Fete A, Reyren N, et al. Two-Dimensional Quantum Oscillations of the Conductance at LaAlO3/SrTiO3 Interfaces. Phys Rev Lett. 2010;105(23).

88. Kalisky B, Bert JA, Klopfer BB, Bell C, Sato HK, Hosoda M, et al. Critical thickness for ferromagnetism in LaAlO3/SrTiO3 heterostructures. Nat Commun. 2012;3.

89. Cowley RA. The phase transition of strontium titanate. Philos Trans R Soc a-Mathematical Phys Eng Sci. 1996;354(1720):2799–814.

90. Mishina ED, Morozov AI, Sigov AS, Sherstyuk NE, Aktsipetrov OA, Lemanov V V, et al. A study of the structural phase transition in strontium titanate single crystal by coherent and incoherent second optical harmonic generation. J Exp Theor Phys. 2002;94(3):552–67.

91. Salje EKH, Gallardo MC, Jimenez J, Romero FJ, del Cerro J. The cubic-tetragonal phase transition in strontium titanate: excess specific heat measurements and evidence for a near-tricritical, mean field type transition mechanism. J Physics-Condensed Matter. 1998;10(25):5535–43.

92. Erlich Z, Frenkel Y, Drori J, Shperber Y, Bell C, Sato HK, et al. Optical Study of Tetragonal Domains in LaAlO3/SrTiO3. J Supercond Nov Magn. 2015;28(3):1017–20.

93. Zubko P, Catalan G, Buckley A, Welche PRL, Scott JF. Strain-gradient-induced polarization in SrTiO3 single crystals. Phys Rev Lett. 2007;99(16).

94. Ahluwalia R, Tagantsev AK, Yudin P, Setter N, Ng N, Srolovitz DJ. Influence of flexoelectric coupling on domain patterns in ferroelectrics. Phys Rev B. 2014;89(17).

95. Pauli SA, Leake SJ, Delley B, Bjorck M, Schneider CW, Schleputz CM, et al. Evolution of the Interfacial Structure of LaAlO3 on SrTiO3. Phys Rev Lett. 2011;106(3).

96. Schwingenschlogl U, Schuster C. Interface relaxation and electrostatic charge depletion in the oxide heterostructure LaAlO3/SrTiO3. Epl. 2009;86(2).